

Master Thesis

Pion-Loop Contribution to the Anomalous Magnetic Moment of the Muon

B.Sc. Jan Haas

October 2013

INSTITUTE FOR THEORETICAL PHYSICS
JUSTUS-LIEBIG-UNIVERSITÄT GIESSEN

Contents

1	Introduction	1
1.1	History of a_μ	3
1.2	Magnetic Moments	4
1.3	Experiment	5
2	Standard Model a_μ	7
3	Framework	13
3.1	Quark DSE	13
3.2	Rainbow-Ladder Truncation	15
3.3	Bethe-Salpeter Equations and T-Matrix	16
3.4	Example: Hadronic Vacuum Polarization	19
4	Hadronic Light-by-Light	21
4.1	Projection	21
4.2	Photon Four-Point Function	24
4.3	Pseudoscalar Exchange	27
4.4	Numerical Implementation I	29
4.5	Charged Pion-Loop	33
4.6	Numerical Implementation II	38
4.7	Results and Discussion	42
5	Conclusion	47
6	Bibliography	49

1 Introduction

The anomalous magnetic moment of the muon a_μ is one of the most precisely measured observables of the Standard Model of particle physics. The high precision of measurement, as well as theoretical prediction, renders a_μ a very interesting test of our understanding of the microscopic world.

The Standard Model consists of three fundamental interactions. The most commonly known of them is the electromagnetic interaction, described by the quantum field theory we call Quantum Electro Dynamics (QED). The current value of the anomalous magnetic moment of the electron a_e is completely mediated by this interaction. It can be treated perturbatively and is calculated straight forward. The two other interactions are the weak and the strong force.

a_μ is sensitive to all three interactions of the Standard Model. The precision of its extraction allows us to study effects mediated by these forces. The impact of the weak force is small but traceable. However, the strong force, described by Quantum Chromo Dynamics (QCD), yields considerable contributions to a_μ . These hadronic contributions are divided in two classes. The bigger QCD contribution is called hadronic vacuum polarization (HVP). The other class was named hadronic light-by-light scattering (HLbL). Due to the non-perturbative nature of QCD, the calculation of its physics is quite involved. That is why most groups resort to effective field theories that use, e.g., mesons as degrees of freedom.

We want to apply an approach to the hadronic light-by-light scattering contribution, based on the functional method of Dyson-Schwinger Equations (DSE). This formulation uses non-perturbative quarks and gluons as degrees of freedom. A great advantage of the functional approach, compared to effective field theories, is the fact that we do not need to separate high and low energy QCD contributions. That would give rise to complications since the photon four-point function is involved. This quantity cannot be clearly assigned to a specific scale. The HLbL contribution in general is an intricate affair. It cannot be related to experimental data, so we are not able to compare results.

The functional approach we use has already been used to calculate the HVP and parts of the HLbL contribution [1–4]. In this thesis, we focus on a class of diagrams we identify with the pion-loop in effective field theories. We investigate the behav-

ior of the contribution to a_μ , depending on $\pi\pi\gamma$ -vertices dressed with different form factors. We want to study the impact of vector meson dominance (VMD) models without and with dependence on the relative pion momentum and compare them to the form factor motivated by our approach. If not stated otherwise, we use Euclidean metric and natural units in all our calculations.

The structure of the thesis is as follows: In the remains of this chapter, we proceed to give a general overview of the history and the basic concepts of the magnetic moment of the muon. Then, we give an example on an experimental extraction method.

Chapter 2 is a compilation of the contributions present in the Standard Model and gives a synopsis of the current values of said contributions. We introduce and motivate a method to theoretically extract a_μ in the Standard Model.

In chapter 3, we present the framework of Dyson-Schwinger (DSE) and Bethe-Salpeter Equations (BSE). We explain the truncation used to solve these equations. Furthermore, we introduce objects like the T -matrix and Bethe-Salpeter amplitudes (BSA) and the approximations we apply.

Chapter 4 is the main part of the thesis. It elaborates on general aspects of the hadronic light-by-light contribution to a_μ , and the photon four-point function $\Pi_{\mu\nu\alpha\beta}$. We explain the steps we took to implement a program to extract the anomalous magnetic moment. We present the findings of the thesis and discuss their behavior.

A short summary and conclusion of the thesis is given in chapter 5.

1.1 History of a_μ

The following explanations are based on [5] and [6]. We will not quote all original sources. These can be found in the references of the cited overviews.

Historically, the anomalous Zeeman effect lead to the discovery of an intrinsic electron spin, corresponding to $g = 2$ in 1925 [7]. In 1928, the Dirac theory predicted the same value for g , valid for any spin 1/2 particle [8]. An experiment in 1947 was the first discovery of an anomalous contribution to the magnetic moment of leptons [9]. Shortly after, theoretical considerations by Schwinger lead to the famous Schwinger correction [10], describing the QED one-loop correction to a_μ .

Later, in 1956, it was found that the sensitivity of leptons to quantum-fluctuations from heavier particles and energy scales, e.g. Λ_{QCD} , scales with the leptons squared mass,

$$\delta a_l = \frac{m_l^2}{M^2}. \quad (1.1)$$

This strengthened the interest of the anomalous magnetic moment of the muon, since its mass is approximately two hundred times the mass of the electron. At this time, the problem was the production of polarized muons. However, with the discovery of parity violation in pion decays [11], it was possible to extract a_μ .

The opportunity to investigate possible 'new physics' contributions, where 'new' described everything beyond QED at that time, triggered an experimental interest. At CERN, measurements of the anomalous magnetic moment of the muon were conducted with the cern cyclotron (1958-1962), and a muon storage ring from 1962 until 1968. The measurements with the storage ring produced a deviation 1.7σ between theory and experiment, which made it necessary to include higher QED loop orders in the calculation. A second muon storage ring at CERN, operation during 1969-1976, was precise enough to measure the first hadronic contribution to a_μ , the hadronic vacuum polarization. With the experiment E821 at Brookhaven, running until 2003, the precision reached a point where even weak interaction contributions needed to be included.

The theoretical precision will be discussed in chapter 2, and a comparison of the current values is presented.

1.2 Magnetic Moments

As in the last section, we follow [5], summarizing the basic understanding of the property 'magnetic moment' and 'anomalous magnetic moment'.

Classically, any particle with charge q and mass m traveling an orbit possesses a magnetic dipole moment $\vec{\mu}_m$ and possibly an electric moment \vec{d}_e . These moments give rise to electromagnetic interaction terms that constitute the Hamiltonian,

$$\mathcal{H} = -\vec{\mu}_m \vec{B} + \vec{d}_e \vec{E}, \quad (1.2)$$

with magnetic and electric fields \vec{B} and \vec{E} . The classical form of a magnetic moment is given by

$$\vec{\mu}_L = \frac{q}{2m} \vec{L}, \quad (1.3)$$

with the angular momentum \vec{L} . If we now consider a particle with intrinsic spin \vec{S} , we have

$$\vec{\mu}_m = g \frac{q}{2m} \vec{S}. \quad (1.4)$$

The gyromagnetic ratio g is defined by (1.4) and is a 'container' for dynamical information. Dirac theory predicts that fermionic g -factors should give the value $g = 2$. We will come back to this in chapter 2. However, experiments found a deviation. Further treatment lead to the anomaly

$$a_l = \frac{g - 2}{2}, \quad (1.5)$$

which we call the anomalous magnetic moment. In the Standard Model, the anomaly arises from corrections in the muon-photon-vertex. We will discuss the contributing effects in more detail in chapter 2.

This anomaly, particularly the anomalous magnetic moment of the muon a_μ , is perfect to do high precision tests of our physical framework, the Standard Model. The muon magnetic moment is better suited than the electron magnetic moment, since heavier particles' contributions to a_l scale with the lepton mass squared. If a precise measurement of the τ magnetic moment would be available, the resulting anomaly would be even better suited to investigate anomalous contributions to the magnetic moment.

1.3 Experiment

The measurement of the anomalous magnetic moment is one of the most precisely known physical quantities in particle physics. For a measurement, one needs polarized muons. They are generally produced by weak pion decays,

$$\pi^\pm \rightarrow \mu^\pm + \nu_\mu. \quad (1.6)$$

Here ν_μ is the muon neutrino or anti-neutrino. Since the neutrino handedness is fixed in the Standard Model, it is possible to produce highly polarized muon beams, that can be trapped in storage rings. In Fig.1.1 we show a schematic view of the Brookhaven $g - 2$ experiment, employing the mentioned storage ring.

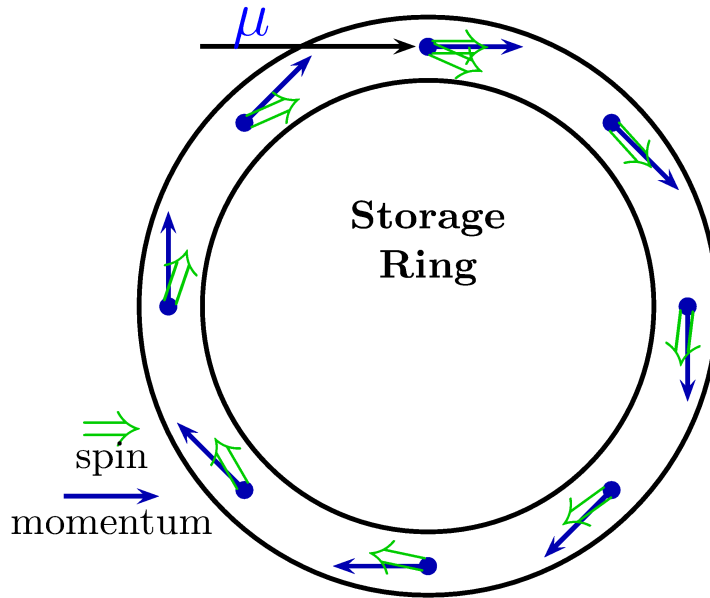


Figure 1.1: Schematic view of the spin precession of polarized muons in a constant magnetic field. (Taken from [5])

The muon is exposed to a magnetic field \vec{B} . With $B = |\vec{B}|$, the anomalous magnetic moment triggers a Larmor precession. The frequency ω_a ,

$$\omega_a = a_\mu \frac{eB}{m_\mu}, \quad (1.7)$$

describes the Larmor precession frequency of the muon spin. While the muon moves with the cyclotron frequency ω_c , the spin has the angular frequency ω_s , where γ is the relativistic Lorentz factor.

$$\omega_c = \frac{eB}{m_\mu \gamma}, \quad (1.8)$$

$$\omega_s = \frac{eB}{m_\mu \gamma} + a_\mu \frac{eB}{m_\mu}. \quad (1.9)$$

In addition, a transversal electric quadrupole field \vec{E} is needed to permanently focus the muons in the storage ring. This field modifies ω_a to

$$\vec{\omega}_a = \frac{e}{m_\mu} \left(a_\mu \vec{B} - \left[a_\mu - \frac{1}{\gamma^2 - 1} \right] \vec{v} \times \vec{E} \right), \quad (1.10)$$

where \vec{v} is the velocity of the muon. At the “magic Energy” $E_{mag} = \gamma m \simeq 3.098$ GeV, the contribution to ω_a depending on the electric field \vec{E} vanishes. This renders E_{mag} a natural choice for the experiment. With this, the necessary quantities to extract a_μ are the magnetic field and ω_a , which is obtained by measuring the decay products of the muon that decays via

$$\mu^\pm \rightarrow e^\pm + \nu_\mu + \bar{\nu}_e, \quad (1.11)$$

with the corresponding neutrino and anti-neutrino. From this, the experimental value of a_μ is extracted [12, 13].

$$a_\mu^{Exp} = 116592089(63) \times 10^{-11}. \quad (1.12)$$

In chapter 2, we will compare this value to the theoretical result to further motivate the investigation of the hadronic contributions to a_μ .

2 Standard Model a_μ

In this chapter, we give an overview of different contributions to the magnetic moment of the muon, considering the Standard Model of particle physics as a frame of reference. We show where the magnetic moment appears in the Standard Model, and introduce the up to date values for QED-, weak interaction- and QCD-contributions. Finally, we compare the extracted values from experiment and theory.

From the theoretical point of view, the magnetic moment is part of the muon interaction with an external magnetic background field. For a relativistic quantum field theory, that means we have to start with the muon-muon-photon vertex Γ_α , defined by

$$\bar{u}(p') \Gamma_\alpha u(p) = \bar{u}(p') \left[\gamma_\alpha F_1(k^2) + \frac{i}{2m_\mu} \sigma_{\alpha\beta} q^\beta F_2(k^2) \right] u(p) \quad (2.1)$$

where $u(p)$ is the muon spinor, k is the photon momentum and $\sigma_{\alpha\beta} = i[\gamma_\alpha, \gamma_\beta]/2$. p and p' are the incoming and outgoing muon momenta. F_1 is the Dirac- or electric form factor and F_2 the Pauli- or magnetic form factor. Charge renormalization leads to

$$F_1(0) = 1. \quad (2.2)$$

From the magnetic form factor at zero momentum, we can extract the anomalous magnetic moment.

$$F_2(0) = a_\mu = \frac{g-2}{2} \quad (2.3)$$

To come to this conclusion, we take a quick look at the matrix element \mathcal{M} . We consider a classical background field A_μ^{cl} ,

$$A_\mu^{cl}(x) = (0, \vec{A}(\vec{x})) \quad (2.4)$$

and, with the help of (2.1), define \mathcal{M} :

$$\mathcal{M} = e \bar{u}(p') \Gamma_\mu u(p) A_\mu^{cl}(\vec{k}), \quad (2.5)$$

with the Fourier transform $A_\mu^{cl}(\vec{k})$ of the field. We can interpret the interaction as a magnetic field $\vec{B}(\vec{k})$ with

$$B^k(\vec{k}) = -i\epsilon^{ijk} k^i A^j(\vec{k}). \quad (2.6)$$

Using the non-relativistic limit

$$u(p) \approx \sqrt{m_\mu} \begin{pmatrix} (1 - \vec{p} \cdot \vec{\sigma}/2m_\mu) \xi \\ (1 + \vec{p} \cdot \vec{\sigma}/2m_\mu) \xi \end{pmatrix}, \quad (2.7)$$

and the limit $k \rightarrow 0$, we arrive at

$$\mathcal{M} = 2m_\mu \frac{e}{m_\mu} [F_1(0) + F_2(0)] \left\langle \frac{\sigma^k}{2} \right\rangle B^k(\vec{k}). \quad (2.8)$$

We can identify this as a Born approximation with the potential V ,

$$V(\vec{x}) = -\langle \vec{\mu} \rangle \cdot \vec{B}(\vec{x}), \quad (2.9)$$

where

$$\langle \vec{\mu} \rangle = \frac{e}{m_\mu} [F_1(0) + F_2(0)] \left\langle \frac{\vec{\sigma}}{2} \right\rangle. \quad (2.10)$$

Comparing this to equation (1.4) with $\vec{S} = \vec{\sigma}/2$ and using (2.2), we find

$$g = 2[F_1(0) + F_2(0)] = 2 + 2F_2(0). \quad (2.11)$$

This is equivalent to (2.3). In Dirac theory, the vertex Γ_α is solely given by

$$\bar{u}(p') \Gamma_\alpha u(p) = \bar{u}(p') \gamma_\alpha F_1(k^2) u(p). \quad (2.12)$$

With $F_2(0) = 0$, we do not have any anomaly, and we have $g = 2$, as mentioned in section 1.2. A more detailed explanation on this comparison can be found in [14] or other text books.

The main tasks are now to extract F_2 from equation (2.1) and to identify all contributions. Projecting out F_2 will be explained for the hadronic light-by-light contribution in section 4.1. In the Standard Model, the contributions to the vertex can be divided in QED-, weak-interaction- and QCD-parts. The biggest share to a_μ is given by the electromagnetic parts, so it is natural to start with QED.

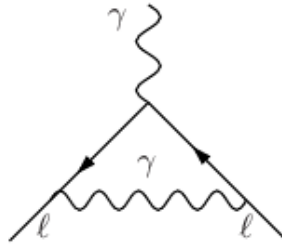


Figure 2.1: QED one-loop diagram. The Schwinger result is the largest correction to the magnetic moment of the muon. It is a general correction, that appears in the magnetic moments of all leptons.

Since QED is weakly coupled, we can sort the QED diagrams by the number of loops, with higher order contributions becoming less significant. The one-loop diagram leads to the famous Schwinger result [10],

$$a_{\mu}^{QED,1L} = \frac{\alpha}{2\pi}, \quad (2.13)$$

extracted from Fig.2.1. For higher loop orders, the number of diagrams grows very fast. At two-loop order, nine diagrams contribute, shown in Fig.2.2. At three-loop order, there are already 72 and at four-loop order around one thousand. Even with this high amount of diagrams, the calculation of the contributions is straight forward. The results are listed in table I.

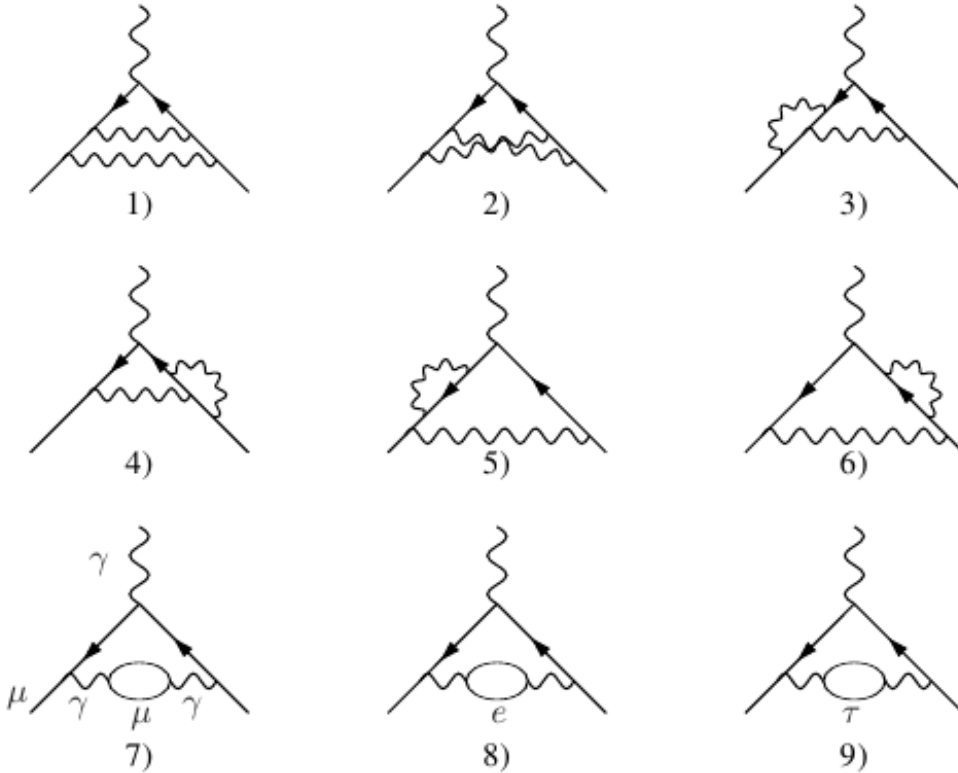


Figure 2.2: QED two-loop diagrams. (Taken from [5])

Loop order	$a_\mu^{QED} [\times 10^{11}]$
2	413217.621(14)
3	30141.902(1)
4	380.807(25)

Table I: Results for the QED contributions to a_μ for two-, three- and four-loop order diagrams.

Recently, even the five-loop order has been published [15], with the result

$$a_\mu^{QED,5L} = 753.29(1.04) \left(\frac{\alpha}{\pi}\right)^5 \approx 5 \times 10^{-11}. \quad (2.14)$$

In equation (2.14) we see, that the five-loop diagrams are suppressed by a factor $(\alpha/\pi)^5$ and we can say that QED is under control.

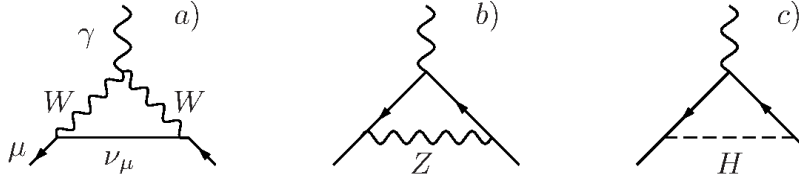


Figure 2.3: Weak one-loop order diagrams. (Taken from [5])

Next, we consider the weak contributions. They are known to two-loop order plus some leading three-loop parts. The value given in [16] is:

$$a_\mu^{weak} = 153.5(1.0) \times 10^{-11}. \quad (2.15)$$

The one-loop order is displayed in Fig.2.3.

The QCD diagrams can be decomposed in two different types of contributions, the hadronic vacuum polarization (HVP) and the hadronic light-by-light scattering. We will discuss the HVP contribution briefly in chapter 3. The HLbL contribution is treated in chapter 4. To summarize the full theoretical value for a_μ^{SM} in the Standard Model, we give their values here and discuss them later. The published values [17,18] are

$$a_\mu^{HVP,LO} = 6949.1(58.2) \times 10^{-11}, \quad (2.16)$$

$$a_\mu^{HVP,HO} = -98.4(1.0) \times 10^{-11}, \quad (2.17)$$

$$a_\mu^{HLbL,EFT} = 105(26) \times 10^{-11}, \quad (2.18)$$

for the HVP leading order, the HVP higher orders and the HLbL contributions from effective field theories. Adding up all of these values we arrive at the Standard Model value

$$a_\mu^{SM} = 116591827(64) \times 10^{-11}, \quad (2.19)$$

compared to the experimental value

$$a_{\mu}^{Exp} = 116592089(63) \times 10^{-11}, \quad (2.20)$$

which leaves an unexplained difference of $\Delta a_{\mu} = 262(89) \times 10^{-11}$. This difference is one of the main reasons why the anomalous magnetic moment is and will be in the next years, a very interesting field of study. It probes the borders of our understanding of particle properties in the Standard Model. If this difference cannot be resolved within the Standard Model, we need to look for new physics contributions, not covered by QED, QCD and weak interaction.

The biggest fraction of the theoretical uncertainty is the hadronic correction. Believing in the errors given in (2.16) to (2.18), the HVP contribution is the most problematic part, but since it can be related to experimental data, we assume that its precision will improve a lot in the future. The biggest problem will then be the HLbL contribution. It cannot be related to experimental data, and the obtained results so far have been calculated in effective field theories. That motivates alternative approaches, like functional methods.

3 Framework

This chapter gives a short overview of the used method, as well as an idea of the used notation. Firstly, we present a schematic manual to calculate the quark propagator and then our truncation. We introduce some objects calculated from Bethe-Salpeter Equations (BSE). Finally, as an example of how to use this framework to calculate contributions to a_μ , we look at the hadronic vacuum polarization (HVP).

The technique we use is a functional method. It generates Dyson-Schwinger Equations (DSE) for propagators and BSEs for vertices and bound state amplitudes. A detailed explanation can, e.g., be found in [19, 20]. DSEs and BSEs are exact, but a problem arises as they are in fact infinite towers of equations. To evaluate them, we have to resort to truncations. A truncation describes a simplification that restricts the calculation to a finite number of equations in order to solve them. The requirement is that it obeys and preserves the given symmetries of the theory. It is important, that we get full non-perturbative propagators and vertices.

3.1 Quark DSE

Since it is one of the main ingredients to calculate hadronic diagrams, we will outline the calculation of the quark propagator in RL truncation.

For the inverse dressed quark propagator, we have to solve the DSE shown in Fig.3.1. In Euclidean metric, we can decompose the inverse quark propagator as given by

$$S^{-1}(p) = Z_f^{-1}(p^2) (-i\not{p} + M(p^2)), \quad (3.1)$$

with the quark wave-function renormalization $Z_f(p^2)$ and the quark mass function $M(p^2)$. This leads to the DSE, which is the equation of motion of the Green's function for the quark,

$$S^{-1}(p) = Z_2 S_0^{-1}(p) + \Sigma(p) \quad (3.2)$$

with the self energy

$$\Sigma(p) = g^2 Z_{1F} C_f \int \frac{d^4 q}{(2\pi)^4} D_{\mu\nu}(p-q) \gamma_\mu S(q) \Gamma_\nu(q, p). \quad (3.3)$$

Z_2 is the quark and Z_{1F} the quark-gluon vertex renormalization factor. The Casimir $C_f = 4/3$ comes from the color trace. The inverse bare quark propagator $S_0^{-1}(p)$ and the gluon propagator $D_{\mu\nu}(p)$ in Landau gauge are denoted by

$$S_0^{-1}(p) = -i\not{p} + m_0. \quad (3.4)$$

$$D_{\mu\nu}(p) = \left(\delta_{\mu\nu} - \frac{p_\mu p_\nu}{p^2} \right) \frac{Z(p^2)}{p^2} \quad (3.5)$$

where m_0 is the bare quark mass. For the fully dressed quark-gluon vertex Γ_μ , and the

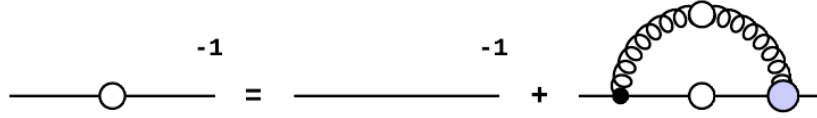


Figure 3.1: Dyson-Schwinger Equation for the quark propagator. The right quark-gluon-vertex as well as the quark and gluon propagator are fully dressed.

gluon dressing, the RL truncation with the MT model is used. Now we can project out $Z_f(p^2)$ and $M(p^2)$ from equation (3.1), and solve the equation numerically.

3.2 Rainbow-Ladder Truncation

A full quark-gluon vertex can be decomposed in twelve Dirac covariants. The $T^{(i)}$ are the tensor structures and the $\lambda^{(i)}$ are their dressing functions.

$$\Gamma_\mu(p, q) = \sum_i^{12} T_\mu^{(i)} \lambda^{(i)}(p, q). \quad (3.6)$$

However, in the Rainbow-Ladder (RL) truncation, the vertex is given only by the 'bare' structure denoted by

$$\Gamma_\mu(k^2) = \gamma_\mu \Gamma^{\text{YM}}(k^2), \quad (3.7)$$

with the scalar dressing function Γ^{YM} as a function of the squared gluon momentum $k^2 = (p - q)^2$. We employ the Maris-Tandy (MT) model to express the phenomenologically observed effective coupling, which is defined by equation (3.8).

$$\begin{aligned} \alpha_{eff}(k^2) &= \frac{g^2}{4\pi} Z(k^2) \Gamma^{\text{YM}}(k^2) \\ &= \frac{\pi}{\omega^6} D k^4 \exp\left(-\frac{k^2}{\omega^2}\right) + \frac{2\pi\gamma_m[1 - \exp(-k^2/(4m_t^2))]}{\log(\tau(1 + k^2/\Lambda_{QCD}^2))}, \end{aligned} \quad (3.8)$$

with $\omega = 0.4$ GeV and $D = 0.93$ GeV². $Z(k^2)$ is the gluon dressing function. The other parameters are $\gamma_m = 12/(33 - 2N_f)$, $m_t = 0.5$ GeV, $\tau = e^2 - 1$ and $\Lambda_{QCD} = 0.234$ GeV, where N_f is the number of quark flavors. The basic idea of the model is, that it should provide an interaction that is strong enough in the infrared to reproduce dynamic chiral symmetry breaking and at the same time approaches the one-loop coupling of QCD for $k^2 \gg \Lambda_{QCD}$. In the standard setting, the parameters ω and D are used to fit the model to the physical pion decay constant f_π .

For some applications it is useful to define the RL interaction kernel K ,

$$K_{rs,tu}(k) = 4\pi \frac{\alpha_{eff}(k^2)}{k^2} T_{\mu\nu}(k) [\gamma_\mu]_{rt} [\gamma_\nu]_{us}, \quad (3.9)$$

where $T_{\mu\nu}$,

$$T_{\mu\nu}(k) = \left(\delta_{\mu\nu} - \frac{k_\mu k_\nu}{k^2} \right), \quad (3.10)$$

is the transverse projector. We use this Kernel in BSE calculations later on.

The Rainbow-Ladder truncation got its name from the fact that the diagrams in RL only consist of planar diagrams without crossing gluons. Pictorial, this results in either rainbow-like, or ladder-like structures. A diagram in RL-truncation is shown later on in Fig.3.8.

3.3 Bethe-Salpeter Equations and T-Matrix

To calculate the HLbL contributions to a_μ , we will employ the T -matrix, Bethe-Salpeter Amplitudes (BSA) and vertices derived from BSEs. In the following, we introduce these objects.

We want to describe a quark-antiquark bound state, so we start with the Green's function

$$G(x_1, x_2, y_1, y_2) = \langle 0 | T \psi(x_1) \bar{\psi}(x_2) \psi(y_1) \bar{\psi}(y_2) | 0 \rangle, \quad (3.11)$$

which contains four external (anti-)quark legs. It can be decomposed in a connected and a disconnected part, as shown in Fig.3.2 for momentum space. In a very shorthand notation, suppressing the indices, it can be written as

$$G = SS + SSTSS, \quad (3.12)$$

with S denoting quark propagators. As we can see in equation (3.12), the T -matrix

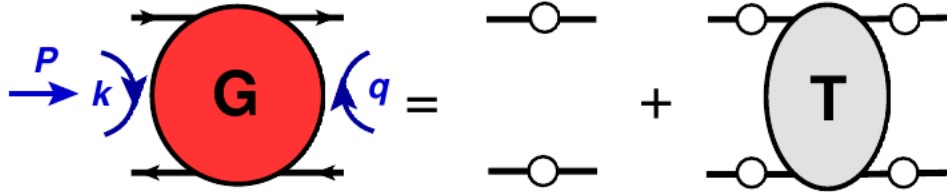


Figure 3.2: This figure shows the decomposition of the G -matrix in a disconnected part and a connected part. The disconnected part consists of two non-interacting dressed quarks. In equation (3.12), it is denoted by SS . The connected part defines the T -matrix, when the dressed quark-legs are amputated. The notation for the connected part in equation (3.12) is $SSTSS$.

is defined as the amputated, connected part of G . To determine T , we use the inhomogeneous BSE for the G -matrix [21],

$$G = SS + GKSS, \quad (3.13)$$

where K is the interaction kernel. This equation can be diagrammatically expressed as Fig.3.3. We combine the equations (3.12) and (3.13), to arrive at the inhomogeneous BSE

$$T = K + TSSK, \quad (3.14)$$

shown in Fig.3.4. Now we use, here in Dirac-metric, the pole-approximation

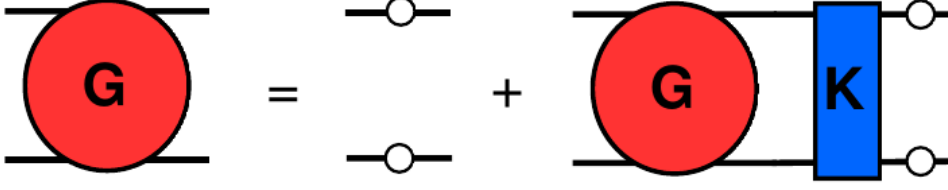


Figure 3.3: Pictorial representation of the inhomogeneous G -matrix BSE. As in Fig.3.2, the disconnected, dressed quarks are denoted SS . The blue box represents the interaction Kernel K . We use the Kernel defined by equation (3.9). The diagram containing the G -matrix and the Kernel is denoted by $GKSS$ in equation (3.13).

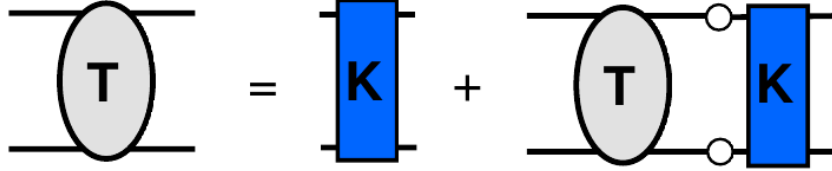


Figure 3.4: The combination of (3.12) and (3.13) lead to the inhomogeneous BSE for the T -matrix. The right hand side of the equation consists of a 'bare' interaction Kernel denoted by K , and a T -matrix connected to a Kernel via dressed quarks, $TSSK$.

$$T(P, k, q) \approx -i \frac{\Gamma(P, k) \bar{\Gamma}(P, q)}{P^2 - m^2}. \quad (3.15)$$

Γ is the Bethe-Salpeter amplitude, and $\bar{\Gamma}$ its conjugate. The mass of the meson pole we want to treat is denoted by m . The pole-approximation assumes that the physical particle masses appear in the T -matrix as poles. These poles are the dominant contributions, so we neglect other terms. Using this expression for T in equation (3.14), we get the homogeneous BSE for Γ , shown in Fig.3.5,

$$\Gamma = \Gamma SSK. \quad (3.16)$$

As a homogeneous equation, we need another normalization condition, that can be retrieved from the G -matrix BSE (3.13). This can be found in [22]. The BSA is an on-shell object. Since the mesons in our calculations are not on-shell, it is necessary to use an off-shell prescription. This was done using the axial-vector WTI (AXWTI) in the chiral limit as a starting point, e.g. in [6].

Another important object that can be calculated in form of a BSE is the quark-

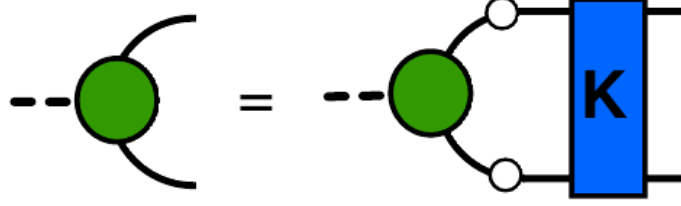


Figure 3.5: Meson bound state BSE, derived from the T -matrix BSE. The green blob represents the Bethe-Salpeter amplitude Γ . In equation (3.16), the diagram containing the dressed quarks and the interaction Kernel K is denoted by ΓSSK .

photon vertex Γ_μ . Its BSE is given by equation (3.17),

$$\Gamma^\mu = \gamma^\mu + \Gamma^\mu SSK, \quad (3.17)$$

and pictorial in Fig.3.6. We find this equation by closing the G -matrix BSEs left side with an outgoing photon. Its tensor structure is the same as the quark-gluon vertex. We can start with equation (3.6) and sort it in transverse and non-transverse parts,

$$\Gamma_\mu(p, q) = \sum_i^{12} T_\mu^{(i)} \lambda^{(i)}(p, q) = \sum_{i=1}^4 T_{\mu,L}^{(i)} \lambda_L^{(i)}(p, q) + \sum_{i=5}^{12} T_{\mu,T}^{(i)} \lambda_T^{(i)}(p, q). \quad (3.18)$$

The four longitudinal components, denoted by the index L , are fixed by WTIs. A discussion of the importance of the transverse parts, denoted by T , can, e.g., be found in [23]. The results obtained by our method do not only reproduce the commonly used Ball-Chiu vertex [24] in its non-transverse part, it also generates transverse structures and satisfies the WTIs.

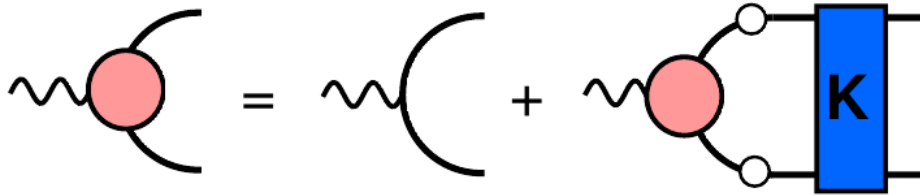


Figure 3.6: This equation describes the inhomogeneous BSE for the quark-photon vertex. The pink blob denotes the vertex. The right side contains a diagram with dressed quarks and the interaction Kernel K . As in the other BSEs, we use the Kernel introduced in equation (3.9).

3.4 Example: Hadronic Vacuum Polarization

As an example of how to use functional methods to calculate $g - 2$, we summarize the calculation of the HVP component, as published and discussed in [3].

The leading order HVP in the DSE/BSE approach is defined as shown in Fig.3.7. Its main component is the photon polarization tensor $\Pi_{\mu\nu}$. Although this object can be directly related to experimental data of e^+e^- -annihilation and τ -decays by the use of dispersion relations, it is a very convenient test to the expected accuracy of results obtained in the HLbL sector with the same approach. In higher order contributions two or more $\Pi_{\mu\nu}$ tensors appear. The tensor itself is given by equation

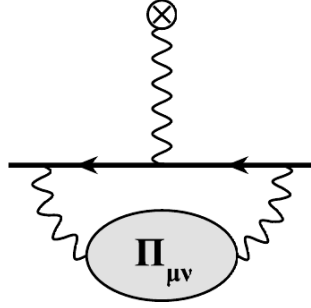


Figure 3.7: Leading order HVP contribution to a_μ .

(3.19), or in terms of diagrams by Fig.3.8. With the help of the propagators $S(p)$ and the quark-photon vertex Γ_μ , calculated as explained in section 3.3, $\Pi_{\mu\nu}$ can be determined.

$$\Pi_{\mu\nu}(P) = Z_2 \int \frac{d^4 q}{(2\pi)^4} \text{Tr} [S(q_-) \Gamma_\mu(P, q) S(q_+) \gamma_\nu] \quad (3.19)$$

with $q_\pm = q \pm P/2$. From the WTI

$$p_\mu \Pi_{\mu\nu}(p) = 0 \quad (3.20)$$

we know that $\Pi_{\mu\nu}$ is transversal. Thus we can write it in terms of a scalar dressing function as in Eq. (3.21).

$$\Pi_{\mu\nu}(p) = \left(\delta_{\mu\nu} - \frac{p_\mu p_\nu}{p^2} \right) p^2 \Pi(p^2) \quad (3.21)$$

$$a_\mu^{HVP} = \frac{\alpha}{\pi} \int_0^1 dx (1-x) \left[-e^2 \Pi_R \left(\frac{x^2}{1-x} m_\mu \right) \right] \quad (3.22)$$

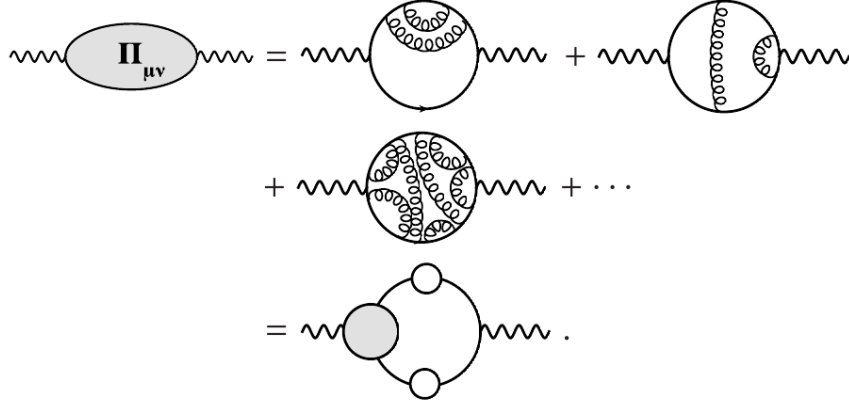


Figure 3.8: Photon self energy tensor in DSE/BSE formalism in RL, as well as in exact notation, without any applied truncation. The left vertex and both quark propagators are fully dressed.

With this, the contribution to a_μ can be extracted from (3.22). Since Π diverges logarithmically, Π_R , the scalar renormalized photon polarization function is used in this equation. For the renormalization, a reasonable choice is

$$\Pi_R(p^2) = \Pi(p^2) - \Pi(0). \quad (3.23)$$

To get an idea of the dependence of a_μ on the quark masses, two different settings were used. Setting *I* was tuned to reproduce the physical pseudoscalar, and setting *II* the vector meson masses. The values obtained by these calculations are

$$a_\mu^{HVP,I} = 7440 \times 10^{-11}, \quad (3.24)$$

$$a_\mu^{HVP,II} = 6760 \times 10^{-11}. \quad (3.25)$$

In comparison, the value derived from dispersion relations, (2.16), is

$$a_\mu^{HVP,disp.} = 6949.1(58.2) \times 10^{-11}.$$

The result with quark masses adjusted to the more relevant vector meson sector is in good agreement with the experiment, which supports the believe that the model is applicable to calculate hadronic contributions of a_μ . Higher order contributions that are so far quoted as (2.17), $a_\mu^{HVP,HO} = -98.4(1.0) \times 10^{-11}$, were not considered yet, however calculations would be feasible.

4 Hadronic Light-by-Light

In this chapter, we want to give an idea of the calculations used to extract the contributions to the anomalous magnetic moment of the muon from hadronic light-by-light scattering. We shortly consider the finiteness of the photon four-point function $\Pi_{\mu\nu\alpha\beta}$, which plays a major role in the calculations. We compare the effective field theory expansion of the four-point function to the functional expansion. For completeness, the quark-loop is discussed. Afterwards, we elaborate on the pseudoscalar exchange contribution, since we apply an analog strategy for the charged pion-loop contribution. We then proceed to explain our numerics. Finally, we apply the mentioned strategy to the charged pion-loop and elaborate on the diagrams included in this contribution. Afterwards we extend the explanations of our numerics to the new four-point function. In the concluding section, we present and discuss the results we obtained.

4.1 Projection

The starting point for our calculation is the muon-muon-photon vertex Γ_μ , as introduced in equation (2.1),

$$\bar{u}(p') \Gamma_\alpha u(p) = \bar{u}(p') \left[\gamma_\alpha F_1(k^2) + \frac{i}{2m_\mu} \sigma_{\alpha\beta} q^\beta F_2(k^2) \right] u(p).$$

We consider the muon being in its rest frame, so the muon-momentum p in Euclidean metric is

$$p = \begin{pmatrix} 0 \\ 0 \\ 0 \\ im_\mu \end{pmatrix}. \quad (4.1)$$

Furthermore, k is the external photon and p' is the resulting muon-momentum after the scattering. In the case of HLbL contributions, the vertex corresponds to Fig.4.1. To extract a_μ , we need to project out $F_2(k^2)$.

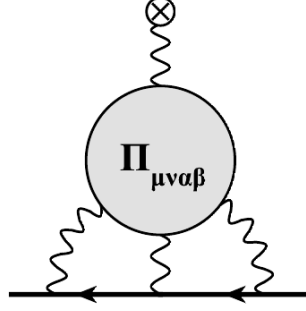


Figure 4.1: The HLbL diagram. From left to right, the internal photon momenta denote q_1, q_2, q_3 , the external momentum is k .

A direct projection method is, for example,

$$F_2(k^2) = \text{Tr} [(\not{p} + m_\mu) \Lambda_\alpha^{(2)} (\not{p}' + m_\mu) \Gamma_\alpha] \quad (4.2)$$

with the projector $\Lambda_\alpha^{(2)}$ [25] given by

$$\Lambda_\alpha^{(2)} = \frac{m_\mu^2}{k^2 (4m_\mu^2 - k^2)} \left[\gamma_\alpha + \frac{k^2 + 2m_\mu^2}{m_\mu (k^2 - 4m_\mu^2)} (p' + p)_\alpha \right]. \quad (4.3)$$

Considering (2.3), we have to evaluate F_2 at zero momentum. It is necessary to take the limit $k^2 \rightarrow 0$. A calculation with $k^2 = 0$ is not possible, because of the structure of the projector. Another problem with this projection is the behavior of the photon four-point function for large photon momenta. We will come to that later. For now, it is important that this projection method is numerically quite involved because of possible divergences in loop contributions.

A method to evade that problem is the usage of the Ward-Takahashi Identities

$$\begin{aligned} q_\nu^{(1)} \Pi(q_1, q_2, q_3)_{\mu\nu\alpha\beta} &= 0 \\ q_\alpha^{(2)} \Pi(q_1, q_2, q_3)_{\mu\nu\alpha\beta} &= 0 \\ q_\beta^{(3)} \Pi(q_1, q_2, q_3)_{\mu\nu\alpha\beta} &= 0 \\ k_\mu \Pi(q_1, q_2, q_3)_{\mu\nu\alpha\beta} &= 0. \end{aligned} \quad (4.4)$$

As long as they hold, they allow us to write [26]

$$\Pi_{\sigma\nu\alpha\beta}(q_1, q_2, q_3) = -k^\mu \frac{\partial}{\partial k^\sigma} \Pi_{\mu\nu\alpha\beta}(q_1, q_2, q_3) \quad (4.5)$$

and

$$\Gamma_\mu = -k^\sigma \tilde{\Gamma}_{\sigma\mu} \quad (4.6)$$

with

$$\begin{aligned}
 ie\tilde{\Gamma}_{\sigma\mu} = & \int \frac{d^4 q_1}{(2\pi)^4} \int \frac{d^4 q_3}{(2\pi)^4} D_{\nu\nu'}(q_1) D_{\alpha\alpha'}(q_2) D_{\beta\beta'}(q_3) \\
 & \times (ie\gamma_{\nu'}) S(p - q_3 - q_2) (ie\gamma_{\alpha'}) S(p - q_3) (ie\gamma_{\beta'}) \\
 & \times \left[(ie)^4 \frac{\partial}{\partial k^\sigma} \Pi_{\mu\nu\alpha\beta}(q_1, q_2, q_3) \right].
 \end{aligned} \tag{4.7}$$

$S(p)$ is the perturbative muon propagator

$$S(p) = \frac{i\not{p} + m_\mu}{p^2 + m_\mu^2} \tag{4.8}$$

and $D_{\mu\nu}$ the photon propagator

$$D_{\mu\nu}(p) = \left(\delta_{\mu\nu} - \frac{p_\mu p_\nu}{p^2} \right) \frac{1}{p^2} + \xi \frac{p_\mu p_\nu}{p^4}. \tag{4.9}$$

ξ is the gauge parameter. We use Landau gauge and Feynman gauge in our calculations, corresponding to $\xi = 0$ and $\xi = 1$. Using the equations (4.7)-(4.9), we are able to directly fix $k = 0$ and extract a_μ ,

$$a_\mu = \frac{1}{48m_\mu} \text{Tr} \left[(i\not{p} + m_\mu) [\gamma_\sigma, \gamma_\mu] (i\not{p} + m_\mu) \tilde{\Gamma}_{\sigma\mu} \right]. \tag{4.10}$$

Since we work with an object like a photon five-point function now, divergences in loops are not present anymore.

We solved this equation numerically for different contributions to $\Pi_{\mu\nu\alpha\beta}(q_1, q_2, q_3)$. We tried the direct method as an independent cross check as well, but due to numerical instabilities, an extraction of reasonable results was not possible.

4.2 Photon Four-Point Function

In Fig.4.2 the idea of a diagrammatical expansion of $\Pi_{\mu\nu\alpha\beta}$ motivated by large- N_c expansion and chiral effective theories [27] is shown. Previous approaches claimed that the individual contributions are different approaches to the same effect and should not be added. In our approach, this question does not arise, since the contributions are generated simultaneously. The expansion displayed in Fig.4.2 has been used to calculate the HLbL contribution to a_μ in the extended Nambu-Jona-Lasinio (ENJL), Hidden Local Symmetry (HLS), vector meson dominance (VMD) and non-local chiral quark models. A summary can be found in Ref. [18]. These models give $a_\mu^{HLbL,EFT} = 105(26) \times 10^{-11}$, as already quoted in chapter 2.

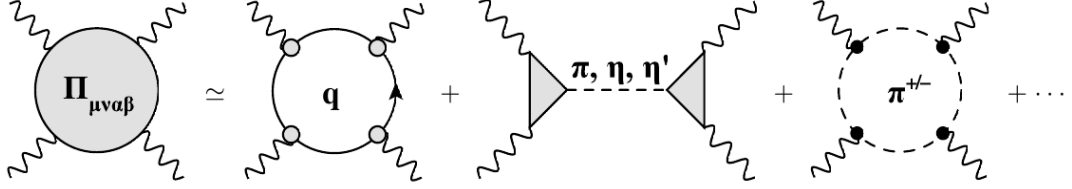


Figure 4.2: Diagrammatical expansion of $\Pi_{\mu\nu\alpha\beta}$. From left to right, the quark-loop, the pseudoscalar meson exchange and the charged pion-loop are shown.

This value is not without controversy. A known and widely discussed problem [5] is the fact that it is necessary to describe the mesons as off-shell particles. This procedure can lead to effective results that are highly model dependent. It is therefore not possible to determine an adequate error. This motivates further investigations with a wide range of different methods. Our fundamental degrees of freedom are

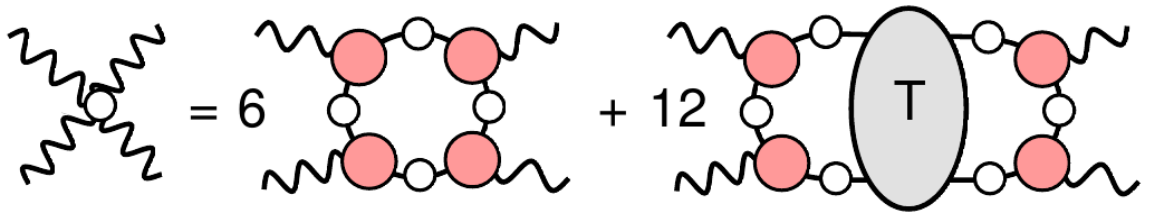


Figure 4.3: Photon four-point function extracted by 'gauging' the hadronic vacuum polarization tensor in RL truncation. The factors indicate the number of permutations we have to consider in the explicit calculation. All quarks and quark-photon vertices are dressed.

dressed quarks and gluons. The photon four-point function is extracted from taking two derivatives of the photon DSE with respect to the photon. This leads to a diagrammatical expression shown in Fig.4.3. The factors indicate how many different

permutations of the object have to be considered. A derivation can be found in [6]. The first diagram in our expansion, Fig.4.4, is the quark-loop. Even though we do not use the calculation of the quark-loop to test our numerics or explain aspects of the process of the calculations used in this thesis, we at least want to mention it for completeness. It can be calculated with the knowledge of the dressed quark propagator and the dressed quark-photon vertex. With this it is possible to extract the $a_\mu^{HLbL, q-Loop}$ contribution. A detailed discussion of the latest efforts to calculate it can be found in [6]. Since we want to focus on the charged pion-loop, we do not further elaborate on the quark-loop. The second diagram in our expansion will be addressed later.

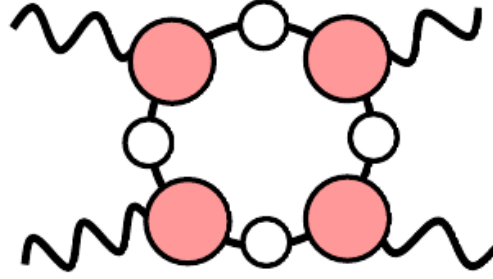


Figure 4.4: The quark-loop part of the photon four-point function, $\Pi_{\mu\nu\alpha\beta}^{q-Loop}$. All quark propagators and all quark-photon vertices are fully dressed.

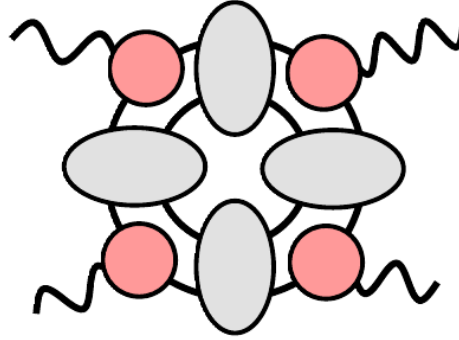


Figure 4.5: The pion-loop contribution shown here is not part of the expansion of the photon four-point function in RL-truncation. For reasons explained in the text, it is reasonable to consider this type of diagram anyway. Because of the limited space, the dressing of the quarks in this figure is omitted. The grey ovals denote T -matrices and the pink dots dressed quark-photon vertices.

What we are interested in is the charged pion-loop shown in Fig.4.5. As we can see, it is not realized in the four-point function in the RL truncation. It would be, if we would consider higher order interactions. Since we know that it will be generated in more realistic approximations, it is nonetheless interesting to calculate its contribution to a_μ , even with an approach that does not generically generate it.

A more general aspect of the four-point function is its structure. Its general tensor structure can be written as [28]

$$\begin{aligned}
\Pi_{\mu\nu\alpha\beta}(q_1, q_2, q_3) = & \Pi_{(1)}(q_1, q_2, q_3)g_{\mu\nu}g_{\alpha\beta} + \Pi_{(2)}(q_1, q_2, q_3)g_{\mu\alpha}g_{\nu\beta} \\
& + \Pi_{(3)}(q_1, q_2, q_3)g_{\mu\beta}g_{\nu\alpha} \\
& + \Pi_{(1)}^{ij}(q_1, q_2, q_3)g_{\mu\nu}q_\alpha^i q_\beta^j + \Pi_{(2)}^{ij}(q_1, q_2, q_3)g_{\mu\alpha}q_\nu^i q_\beta^j \\
& + \Pi_{(3)}^{ij}(q_1, q_2, q_3)g_{\mu\beta}q_\nu^i q_\alpha^j + \Pi_{(4)}^{ij}(q_1, q_2, q_3)g_{\nu\alpha}q_\mu^i q_\beta^j \quad (4.11) \\
& + \Pi_{(5)}^{ij}(q_1, q_2, q_3)g_{\nu\beta}q_\mu^i q_\alpha^j + \Pi_{(6)}^{ij}(q_1, q_2, q_3)g_{\alpha\beta}q_\mu^i q_\nu^j \\
& + \Pi_{(1)}^{ijkl}(q_1, q_2, q_3)q_\mu^i q_\nu^j q_\alpha^k q_\beta^l
\end{aligned}$$

Here the three momenta q_1, q_2, q_3 are the independent internal photon momenta. The external momentum is defined by $0 = k + q_1 + q_2 + q_3$. All combinations $i, j, k, l = 1, 2, 3$ are possible, so the overall number of tensor structures is 138. In fact these structures are not fully independent. With the help of the WTIs (4.5), it is possible to express the complete four-point function as a linear combination of $\Pi_{(1)}^{ijkl}$. The importance of this feature becomes clear, if we consider the canonical dimension D of $\Pi_{\mu\nu\alpha\beta}$. Since $D = 0$, we naively expect divergences in loop contributions. But since $\Pi_{(1)}^{ijkl}$ is accompanied by four momenta q_i , the amplitudes dimension is supposed to be $D = -4$. Thus the result is finite. This is one way to express the decrease of the naive degree of divergence via gauge symmetry effects.

As mentioned in section 4.1, loop contributions pose a numerical problem because of naive divergences. In the case of the quark-loop, we have to consider six different possible permutations of the diagram and all of them diverge logarithmically in the direct projection method. However, the sum of these diagrams is supposed to be finite. The need to work with diagrams with canceling divergences renders these calculations numerically difficult. We will consider the situation for the pion-loop in section 4.5.

4.3 Pseudoscalar Exchange

In section 4.2 we explained which HLbL contributions we want to consider. Next, we show how to apply the approximation for the T -matrix, and arrive at diagrams similar to effective field theories with $PS\gamma\gamma$ form factors. Since we employ a similar strategy for the charged pion-loop, we roughly explain the necessary steps for the pseudoscalar exchange.

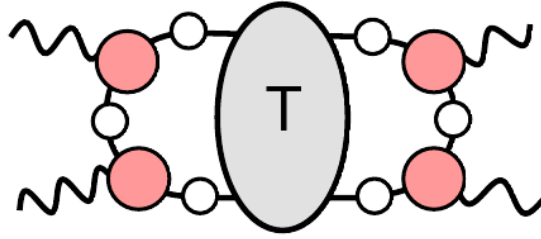


Figure 4.6: PS exchange diagram in the DSE/BSE approach. Pink blobs are dressed quark-photon vertices. All quarks are dressed.

The second diagram in Fig.4.3 has been calculated in the DSE/BSE approach [1, 2]. The corresponding four-point function is represented by Fig.4.6. With the T -matrix approximation (3.15), we can draw the diagram as depicted by Fig.4.7. We can see the similarity to effective field theories when we introduce the $PS\gamma\gamma$ form factor, pictorial represented by Fig.4.8. With this notation, the four-point function can be drawn as Fig.4.9. This corresponds basically to an effective field theory diagram with a form factor.

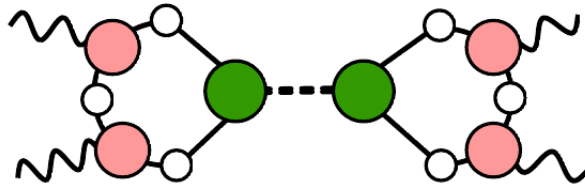


Figure 4.7: PS exchange diagram with applied pole-approximation for the T -matrix. The green blobs are Bethe-Salpeter amplitudes. All quarks are dressed. The pink blobs are dressed quark-photon vertices.

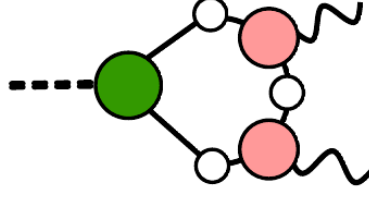


Figure 4.8: $PS\gamma\gamma$ form factor. We collect the Bethe-Salpter amplitude, the dressed quarks and the dressed vertices and define a form factor.

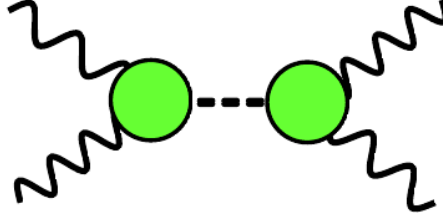


Figure 4.9: PS exchange diagram with $PS\gamma\gamma$ form factors, represented by light green blobs. What is left, is a diagram with two $PS\gamma\gamma$ -vertices, dressed with the form factors.

The extracted value for the PS-exchange contribution to a_μ is

$$a_\mu^{PS} = (80.7 \pm 12.0) \times 10^{-11}. \quad (4.12)$$

As we identified the contribution as PS-exchange, we can compare the result with previous calculations in other approaches. Typical results in the HLS or the ENJL model are [28, 29]

$$a_\mu^{ENJL} = 85(15) \times 10^{-11} \quad (4.13)$$

$$a_\mu^{HLS} = 83(6) \times 10^{-11} \quad (4.14)$$

We see that the DSE/BSE results are consistent with other models. A comparison with more effective field theory results can be found in [6].

4.4 Numerical Implementation I

Since all HLbL contributions have the same structure except for the four-point function, the PS exchange gives us the possibility to test our numerics even if we recalculate effective theory diagrams.

Following [30], we evaluated $a_\mu^{\pi_0}$ for lowest meson dominance (LMD) and a vector meson dominance form factor (VMD), involving either one or two vector resonances in the photons. Sticking to the notation in [30], we write all expressions in terms of q_1 and q_2 . However, in our calculations, we use q_1 and q_3 as independent momenta, with the relation

$$q_2 = -(q_1 + q_3 + k), \quad (4.15)$$

since this momentum routing lead to the quickest numerical convergence of all tested scenarios. The form factors, as well as the derivative of the four-point function, are given in the Dirac metric,

$$\mathcal{F}_{\pi_0\gamma^*\gamma^*}^{LMD}(q_1^2, q_2^2) = \frac{f_\pi}{3} \frac{q_1^2 + q_2^2 - c_V}{(q_1^2 - M_V^2)(q_2^2 - M_V^2)}, \quad (4.16)$$

$$\mathcal{F}_{\pi_0\gamma^*\gamma^*}^{VMD}(q_1^2, q_2^2) = -\frac{N_C}{12\pi^2 f_\pi} \frac{M_V^2}{(q_1^2 - M_V^2)} \frac{M_V^2}{(q_2^2 - M_V^2)}. \quad (4.17)$$

N_C is the number of colors used. $M_V = M_\rho$ is the vector meson mass used in the dominance models, and the constant c_V appearing in (4.16) is given by

$$c_V = \frac{N_C}{4\pi^2} \frac{M_V^4}{f_\pi^2}. \quad (4.18)$$

We will not discuss the behavior of these form factors in detail, since we only use them to test the numerics of our code up to the four-point function with the well known results for the pion exchange. In the case of the pion-loop, the derivative of $\Pi_{\mu\nu\alpha\beta}$ is taken numerically but for the pion exchange, Ref. [30] gives an analytical function

$$\begin{aligned} \frac{\partial}{\partial k^\rho} \Pi_{\mu\nu\lambda\sigma}^{\pi_0}(q_1, q_2, k) &= i \frac{\mathcal{F}_{\pi_0\gamma^*\gamma^*}(q_1^2, q_2^2) \mathcal{F}_{\pi_0\gamma^*\gamma^*}((q_1 + q_2)^2, 0)}{(q_1 + q_2)^2 - M_\pi^2} \epsilon_{\mu\nu\alpha\beta} q_1^\alpha q_2^\beta \epsilon_{\lambda\sigma\rho\tau} (q_1 + q_2)^\tau \\ &+ i \frac{\mathcal{F}_{\pi_0\gamma^*\gamma^*}(q_1^2, 0) \mathcal{F}_{\pi_0\gamma^*\gamma^*}(q_2^2, (q_1 + q_2)^2)}{q_1^2 - M_\pi^2} \epsilon_{\mu\sigma\tau\rho} q_1^\tau \epsilon_{\nu\lambda\alpha\beta} q_1^\alpha q_2^\beta \\ &+ i \frac{\mathcal{F}_{\pi_0\gamma^*\gamma^*}(q_1^2, (q_1 + q_2)^2) \mathcal{F}_{\pi_0\gamma^*\gamma^*}(q_2^2, 0)}{q_2^2 - M_\pi^2} \epsilon_{\mu\lambda\alpha\beta} q_1^\alpha q_2^\beta \epsilon_{\nu\sigma\rho\tau} q_2^\tau \\ &+ \mathcal{O}(k). \end{aligned} \quad (4.19)$$

Since we only evaluate the derivative of the four-point function at $k = 0$, the additional terms $\mathcal{O}(k)$ are not relevant. The results for the pion exchange contribution to a_μ given in [30] are

$$a_\mu^{LMD} = 73 \times 10^{-11}, \quad (4.20)$$

$$a_\mu^{VMD} = 56 \times 10^{-11}. \quad (4.21)$$

We can test our numerics by comparing our results to these values. Later, we can use the same code to evaluate the pion-loop with a simple change of the used derivative of the four-point function.

First we have to convert form factors and four-point function in Euclidean metric. The integration is supposed to cover the entire momentum space of q_1 as well as q_3 . It is convenient to use hyperspherical coordinates, so that the integration to infinity has to be considered only for the radii r_1 and r_3 . The integration measure of a four momentum q ,

$$q = r_q \begin{pmatrix} \sqrt{1 - z_q^2} \sqrt{1 - y_q^2} \sin(\phi_q) \\ \sqrt{1 - z_q^2} \sqrt{1 - y_q^2} \cos(\phi_q) \\ \sqrt{1 - z_q^2} y_q \\ z_q \end{pmatrix} \quad (4.22)$$

in hyperspherical coordinates is given by

$$\int \frac{d^4 q}{(2\pi)^4} = \frac{1}{(2\pi)^4} \int_0^\infty dr_q r_q^3 \int_{-1}^1 dz_q \sqrt{1 - z_q^2} \int_{-1}^1 dy_q \int_0^{2\pi} d\phi_q. \quad (4.23)$$

Since in fact only five independent variables appear, it is possible to evaluate three integrals trivially. We choose

$$q_1 = r_1 \begin{pmatrix} 0 \\ 0 \\ \sqrt{1 - z_1^2} \\ z_1 \end{pmatrix}, \quad q_3 = r_3 \begin{pmatrix} 0 \\ \sqrt{1 - z_3^2} \sqrt{1 - y_3^2} \\ \sqrt{1 - z_3^2} y_3 \\ z_3 \end{pmatrix}, \quad (4.24)$$

so our free variables are r_1, r_3, z_1, z_3 and y_3 . For the integration, we use the Monte Carlo integrator VEGAS [31]. It integrates functions over the unit cube of the

chosen dimension. To cover the Euclidean momentum space, we need to use a coordinate transformation, specified by

$$r_1 = \Lambda_1 \exp \left[\log \left[\frac{\Lambda_2}{\Lambda_1} \right] x_1 \right], \quad (4.25)$$

$$z_1 = 2x_2 - 1, \quad (4.26)$$

$$r_3 = \Lambda_1 \exp \left[\log \left[\frac{\Lambda_2}{\Lambda_1} \right] x_3 \right], \quad (4.27)$$

$$z_3 = 2x_4 - 1, \quad (4.28)$$

$$y_3 = 2x_5 - 1. \quad (4.29)$$

The x_i are the VEGAS internal Cartesian coordinates. If we want to use the transformation, we have to include its Jacobian determinant $\mathcal{J}_{q_1 q_3}^{VEGAS}$

$$\mathcal{J}_{q_1 q_3}^{VEGAS} = 2^3 \cdot \left(\log \left[\frac{\Lambda_2}{\Lambda_1} \right] \right)^2 \cdot r_1 \cdot r_3. \quad (4.30)$$

Λ_1 and Λ_2 are infrared and ultraviolet cutoffs, necessary to integrate the interval zero to “infinity” logarithmically. Values $\Lambda_1 = 10^{-6} - 10^{-3}$ and $\Lambda_2 = 10^3 - 10^6$ have been tested and no relevant deviations in the results were noticed.

The additional factor c_1 for the neglected variables z_1 , ϕ_1 and ϕ_3 results in

$$c_1 = (2\pi)^2 \cdot 2. \quad (4.31)$$

Summarizing all of this, we have to evaluate (4.10),

$$a_\mu = \frac{1}{48m_\mu} \text{Tr} \left[(i\not{p} + m_\mu) [\gamma_\sigma, \gamma_\mu] (i\not{p} + m_\mu) \tilde{\Gamma}_{\sigma\mu} \right],$$

again with (4.15)

$$q_2 = -(q_1 + q_3 + k),$$

and (4.7)

$$\begin{aligned} ie\tilde{\Gamma}_{\sigma\mu} &= \frac{c_1}{(2\pi)^8} \prod_{i=1}^5 \left(\int_0^1 dx_i \right) r_1^3 r_3^3 \sqrt{1 - z_1^2} \sqrt{1 - z_3^2} \\ &\times \mathcal{J}_{q_1 q_3}^{VEGAS} D_{\nu\nu'}(q_1) D_{\alpha\alpha'}(q_2) D_{\beta\beta'}(q_3) \\ &\times (ie\gamma_{\nu'}) S(p - q_3 - q_2) (ie\gamma_{\alpha'}) S(p - q_3) (ie\gamma_{\beta'}) \\ &\times \left[(ie)^4 \frac{\partial}{\partial k^\sigma} \Pi_{\mu\nu\alpha\beta}(q_1, q_2, q_3) \right] \end{aligned}$$

and the derivative of the four-point function given by (4.19), translated to Euclidean metric. For the calculations, we used the definition of the electromagnetic coupling α to express the elementary charge e . We are left with

$$e^6 = 2^3 \cdot (2\pi)^3 \cdot \alpha^3. \quad (4.32)$$

The results lead to

$$a_\mu^{LMD} = 73.3(0.1) \times 10^{-11}, \quad (4.33)$$

$$a_\mu^{VMD} = 56.4(0.1) \times 10^{-11}. \quad (4.34)$$

As one can see, the values are in very good agreement with the reference values (4.20) and (4.21), even though Ref. [30] performed the angular integrations with the help of Gegenbauer polynomials. We consider this as a check of the basic validity of our code. The errors given for our results merely represents the numerical uncertainty of the integration. It does not represent the accuracy of the used method to calculate a_μ .

4.5 Charged Pion-Loop

In this section we consider the charged pion-loop. As mentioned before, the only change to the previous situation is the four-point function.

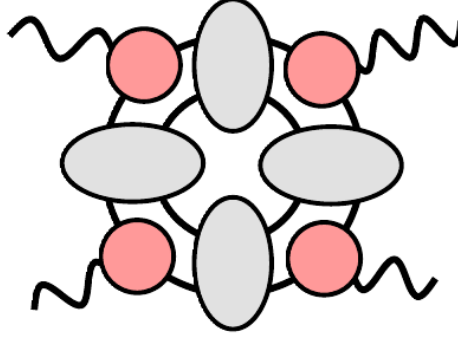


Figure 4.10: This diagram, already shown in Fig.4.5, corresponds to the part of the pion-loop diagrams we are able to solve at the moment.

The diagram we can solve at the moment is shown in Fig.4.10. As before, we use the T -matrix approximation motivated in section 3.3. We can separate the T -matrix in its poles for different physical masses m . Since the pole with the lowest possible mass is the pion, we assume, that

$$T(P, k, q) \approx -i \frac{\Gamma(P, k) \bar{\Gamma}(P, q)}{P^2 - m_\pi^2} \quad (4.35)$$

is a reasonable approximation. With this representation, we can combine two T -matrices as illustrated in Fig.4.11.

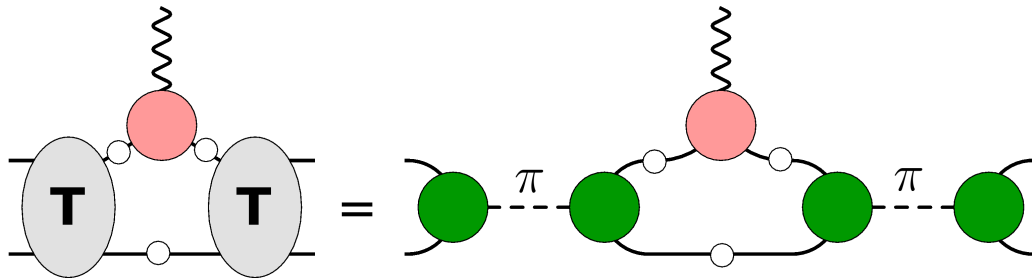


Figure 4.11: Combination of two T -matrices in pole-approximation. When we apply it to the diagram Fig.4.10, we end up with a pion-loop. The green blobs represent Bethe-Salpeter amplitudes. All quarks are dressed, as well as the quark-photon vertex, depicted as a pink blob.

Now we absorb BSAs pairwise into a $\pi\pi\gamma$ form factor, see Fig.4.12. The vertex structure with the form factor is

$$\Gamma_{\mu}^{\pi\pi\gamma}(p_1, p_2) = \mathcal{F}_1^{\pi\pi\gamma}(p_1, p_2) \cdot (p_1 + p_2)^{\mu} + \mathcal{F}_2^{\pi\pi\gamma}(p_1, p_2) \cdot (p_1 - p_2)^{\mu}. \quad (4.36)$$

However, the numerical values for F_2 was so small that we neglected it in further calculations. What we are left with is, up to the form factor, the same expression as the pion propagator S_{π} in scalar QED (sQED),

$$S_{\pi}(p) = \frac{-1}{p^2 + M_{\pi}^2}. \quad (4.37)$$

This theorie describes charged scalar fields. An example for these fields are the pions. In this case, the theorie contains π^+ , π^- and photons. The only vertices that can exist are the $\pi\pi\gamma$ -, and the $\pi\pi\gamma\gamma$ -vertex. The expressions for the vertices are given in section 4.4.

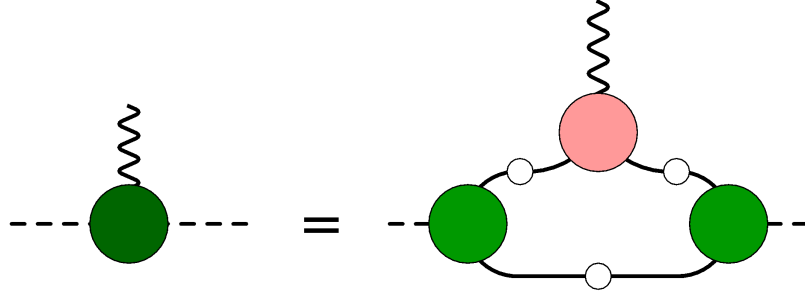


Figure 4.12: We define the $\pi\pi\gamma$ form factor, dark green blob. It consists of two Bethe-Salpeter amplitudes (green blobs) connected by dressed quarks and a dressed quark-photon vertex (pink blob).

A diagrammatical illustration is shown in Fig.4.13. This is why we identify Fig.4.10 as the pion-loop. Because of the similarity, it is useful to first calculate and compare results with sQED, where the pion is treated as a fundamental particle.

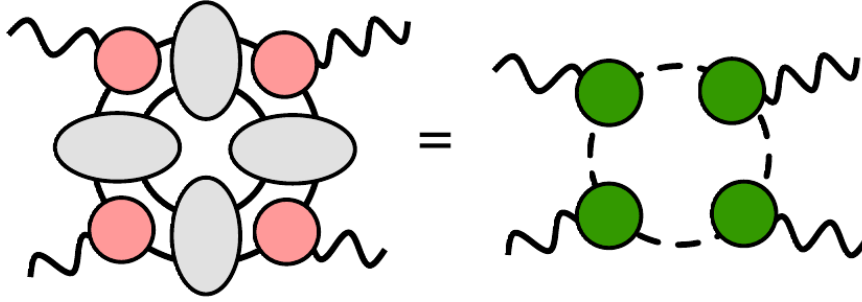


Figure 4.13: With the help of the $\pi\pi\gamma$ -vertex, we are able to consider Fig.4.10 as a pion-loop in scalar QED with an additional form factor for every $\pi\pi\gamma$ -vertex.

In sQED, we have a total of 21 diagrams contribution to a_μ^{HLbL} , containing a pion-loop. These diagrams can be decomposed into three gauge invariant groups, as done in [32]. These groups A , B and C (corresponding to (a),(b),(c)) are shown in Fig.4.14. The factors arise from charge-conjugation and time-reversal invariance. The diagrams that are most important for us are $C3$ and $C4$. These are the contribu-

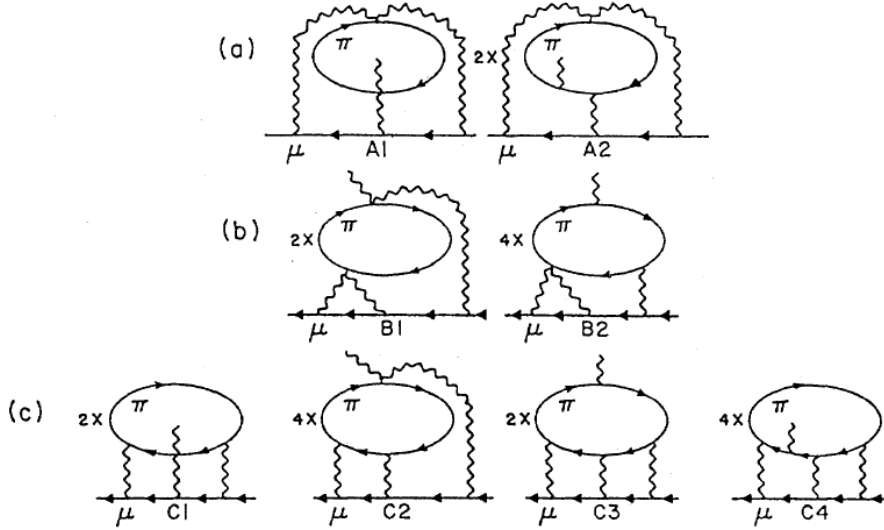


Figure 4.14: Contribution to a_μ^{HLbL} containing the charged pion-loop in scalar QED. The diagrams $C3$ and $C4$ are important for us, since the diagrams we can solve reduce to them in the case of bare vertices. (Taken from [32])

tions that corresponde to our diagrams, assuming the $\pi\pi\gamma$ -vertices to be bare. The rest of the diagrams contain a $\pi\pi\gamma\gamma$ -vertex, we cannot yet include in our calculation.

These diagrams are important to preserve gauge invariance. We will come to this problem in section 4.7.

For the group C , the aquired values in [32] are

$$a_\mu^C = 0.3737(35) \left(\frac{\alpha}{\pi}\right)^3 \approx 468.7 \times 10^{-11} \quad (4.38)$$

with the use of Feynman parametrisation integrals, and

$$a_\mu^C = 0.3772(18) \left(\frac{\alpha}{\pi}\right)^3 \approx 473.1 \times 10^{-11} \quad (4.39)$$

with the same method, applying the WTI (4.5) as we did, for bare vertices. However, because of the derivative, we cannot use the time-reversal invariance for every momentum routing carelessly. With, e.g., a routing as depicted in Fig.4.15, the derivative of diagram $C2a$ is zero, since the external photon does not enter the calculation. Therefore diagram $C2b$ has to be calculated seperatly. In this case, the calculation is not time-reversal invariant.

This similarity provides another tool to test our numerics. Therefore, we include the bare four-vertex diagrams for the moment. The four-point function for all diagrams in C is then

$$\Pi_{\mu\nu\alpha\beta}^C(q_1, q_2, q_3, l) = \sum_{i=1}^4 \eta_i \int \frac{d^4 l}{(2\pi)^4} \mathcal{D}_{\mu\nu\alpha\beta}^i(q_1, q_2, q_3, l), \quad (4.40)$$

where the $\mathcal{D}_{\mu\nu\alpha\beta}^i$ represent the four-point functions of the different diagrams, and η_i the multiplicity. The additional momentum l is the loop momentum. The expressions for the diagrams will be discussed in the next section.

Before we start with further explanations of the performed work, we want to discuss the divergence behavior of the pion-loop. Naively, we start with counting powers of momentum. Every propagator contributes

$$S_\pi \propto \frac{1}{p^2}, \quad (4.41)$$

every bare sQED vertex

$$\Gamma \propto p, \quad (4.42)$$

and the integration measure \mathcal{M} of the loop integral

$$\mathcal{M} \propto p^3. \quad (4.43)$$

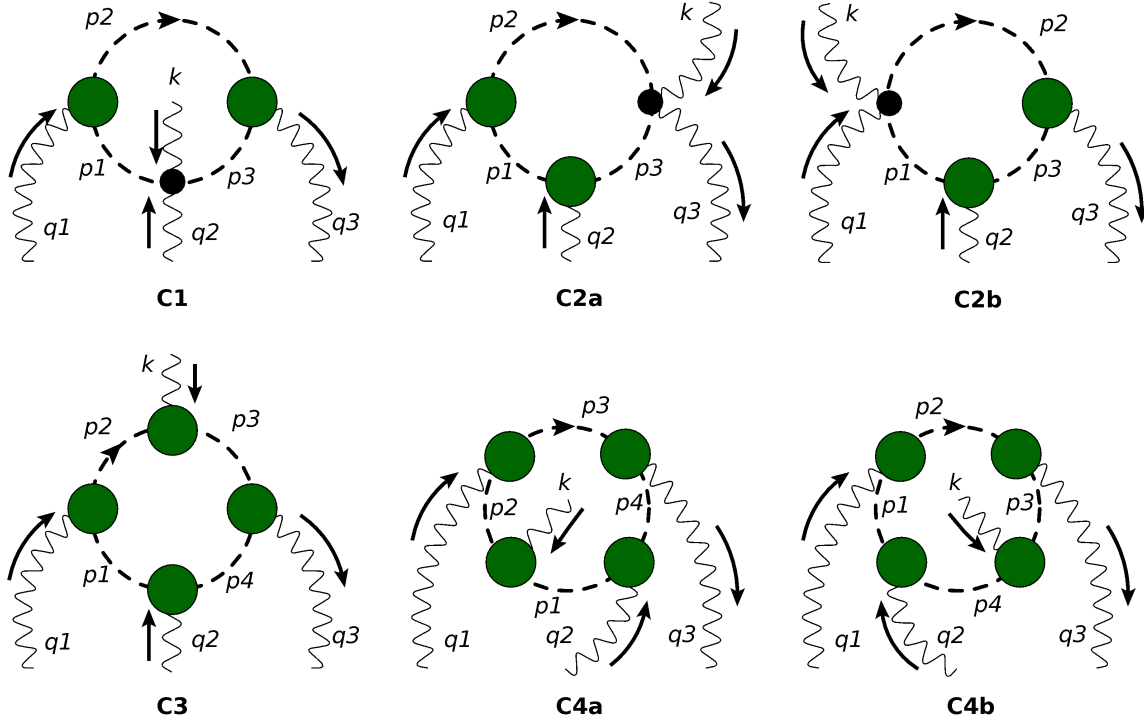


Figure 4.15: This is an example, how routing can affect the time-reversal invariance in the calculation of the pion-loop contribution to a_μ with the derivative of the photon four-point function. With this routing, we have to consider both diagrams $C2a$ and $C2b$ because of the derivative, since the diagram $C2a$ is independent of the external momentum k . The dark green blobs are $\pi\pi\gamma$ -vertices dressed with the different form factors, and the smaller black dots represent the bare $\pi\pi\gamma\gamma$ -vertices.

Considering the whole pion-loop diagram, we end up with

$$\Pi \propto \left(\frac{1}{p^2}\right)^4 \cdot p^4 \cdot p^3 = \frac{1}{p}, \quad (4.44)$$

thus we expect logarithmical divergence. If we now include form factors, the vertices contributions to the power counting change. In fact, we can assume, that at least one of the four vertices provides a dimensionality of $1/p^2$ or better. That is enough to arrive at a finite result.

4.6 Numerical Implementation II

As stated in section 4.4, we use the same code as for the pion exchange. The only thing we have to change is the derivative of the four-point function. To calculate it, we use (4.37) for the pion propagators. The $\pi\pi\gamma$ -vertex is given by

$$\Gamma_{\mu}^{\pi\pi\gamma}(p_1, p_2) = \mathcal{F}^{\pi\pi\gamma}(p_1, p_2) \cdot (p_1 + p_2)^{\mu}, \quad (4.45)$$

where p_1 and p_2 denote the pion momenta. In sQED, the form factor does not exist, so we write

$$\mathcal{F}_{sQED}^{\pi\pi\gamma}(p_1, p_2) = 1 \quad (4.46)$$

for now. The momentum independent sQED $\pi\pi\gamma\gamma$ -vertex is given by

$$\Gamma_{\mu\nu}^{\pi\pi\gamma\gamma} = 2\delta_{\mu\nu}. \quad (4.47)$$

With this, we can calculate the four-point functions of the diagrams. One possible momentum routing is given by

$$\begin{aligned} \mathcal{D}_{\mu\nu\alpha\beta}^1(q_1, q_2, q_3, l) &= S_{\pi}(l)\Gamma_{\nu}^{\pi\pi\gamma}(l, l+q_1)S_{\pi}(l+q_1)\Gamma_{\beta}^{\pi\pi\gamma}(l+q_1, l+q_1+q_3) \\ &\times S_{\pi}(l+q_1+q_3)\Gamma_{\mu\alpha}^{\pi\pi\gamma\gamma}, \end{aligned} \quad (4.48)$$

$$\begin{aligned} \mathcal{D}_{\mu\nu\alpha\beta}^2(q_1, q_2, q_3, l) &= S_{\pi}(l)\Gamma_{\nu}^{\pi\pi\gamma}(l, l+q_1)S_{\pi}(l+q_1)\Gamma_{\mu\beta}^{\pi\pi\gamma\gamma}S_{\pi}(l+q_1+q_3+k) \\ &\times \Gamma_{\alpha}^{\pi\pi\gamma}(l+q_1+q_3+k, l), \end{aligned} \quad (4.49)$$

$$\begin{aligned} \mathcal{D}_{\mu\nu\alpha\beta}^3(q_1, q_2, q_3, l) &= S_{\pi}(l)\Gamma_{\nu}^{\pi\pi\gamma}(l, l+q_1)S_{\pi}(l+q_1)\Gamma_{\mu}^{\pi\pi\gamma}(l+q_1, l+q_1+k) \\ &\times S_{\pi}(l+q_1+k)\Gamma_{\beta}^{\pi\pi\gamma}(l+q_1+k, l+q_1+q_3+k) \\ &\times S_{\pi}(l+q_1+q_3+k)\Gamma_{\alpha}^{\pi\pi\gamma}(l+q_1+q_3+k, l), \end{aligned} \quad (4.50)$$

$$\begin{aligned} \mathcal{D}_{\mu\nu\alpha\beta}^4(q_1, q_2, q_3, l) &= S_{\pi}(l)\Gamma_{\mu}^{\pi\pi\gamma}(l, l+k)S_{\pi}(l+k)\Gamma_{\nu}^{\pi\pi\gamma}(l+k, l+q_1+k) \\ &\times S_{\pi}(l+q_1+k)\Gamma_{\beta}^{\pi\pi\gamma}(l+q_1+k, l+q_1+q_3+k) \\ &\times S_{\pi}(l+q_1+q_3+k)\Gamma_{\alpha}^{\pi\pi\gamma}(l+q_1+q_3+k, l), \end{aligned} \quad (4.51)$$

With this routing, we do not have the mentioned problem with the derivative. It is shown in Fig.4.16. To arrive at the full pion-loop four-point function, we have to integrate over the loop momentum. We do this in hyperspherical coordinates via VEGAS. l is given by

$$l = r_l \begin{pmatrix} \sqrt{1-z_l^2}\sqrt{1-y_l^2}\sin(\phi_l) \\ \sqrt{1-z_l^2}\sqrt{1-y_l^2}\cos(\phi_l) \\ \sqrt{1-z_l^2} \\ z_l \end{pmatrix}. \quad (4.52)$$

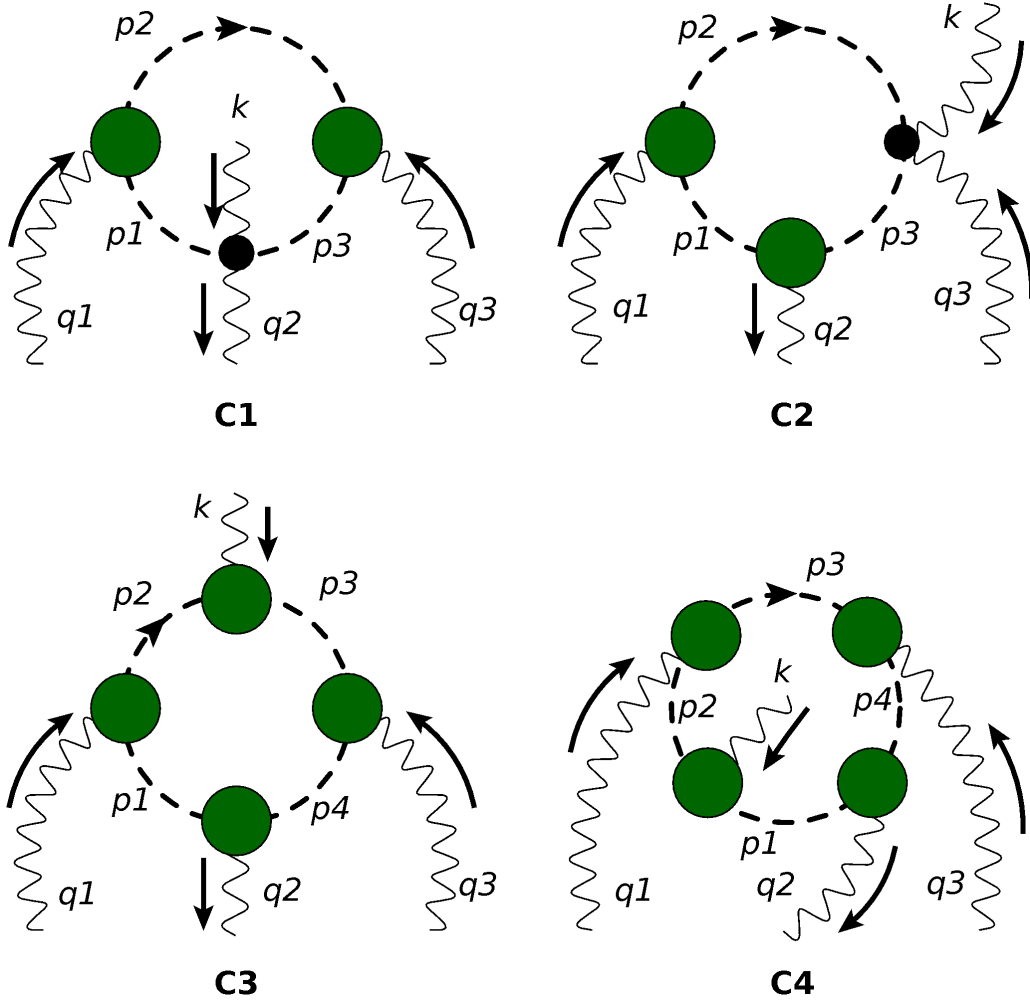


Figure 4.16: We used this momentum routing in our calculations. Time-reversal invariance is no problem here, since we do not use it for diagram *C1*, which we choose to be independent of k . The dark green blobs are $\pi\pi\gamma$ -vertices dressed with the different form factors. We represent the bare $\pi\pi\gamma\gamma$ -vertices with smaller black dots.

As for the previous integrations, we transform into hyperspherical coordinates, and then into VEGAS-coordinates, x_i . The l -integral then is

$$\int \frac{d^4 l}{(2\pi)^4} = \frac{1}{(2\pi)^4} \prod_{i=6}^9 \left(\int_0^1 dx_i \right) r_l^3 \sqrt{1 - z_l^2} \cdot \mathcal{J}_l^{VEGAS}, \quad (4.53)$$

with the transformation specification

$$r_l = \Lambda_1 \exp \left[\log \left[\frac{\Lambda_2}{\Lambda_1} \right] x_6 \right], \quad (4.54)$$

$$z_l = 2x_7 - 1, \quad (4.55)$$

$$y_l = 2x_8 - 1, \quad (4.56)$$

$$\phi_l = 2\pi x_9, \quad (4.57)$$

and the Jacobian determinant

$$\mathcal{J}_l^{VEGAS} = 2^2 \cdot 2\pi \cdot \log \left[\frac{\Lambda_2}{\Lambda_1} \right] \cdot r_l. \quad (4.58)$$

The Λ are the same as before. We take the derivative numerically, using

$$\frac{\partial}{\partial k^\sigma} \Pi_{\mu\nu\alpha\beta}^C(q_2) = \frac{\Pi_{\mu\nu\alpha\beta}^C(q_2 + \epsilon e_\sigma) - \Pi_{\mu\nu\alpha\beta}^C(q_2 - \epsilon e_\sigma)}{2\epsilon}, \quad (4.59)$$

where $\epsilon = 10^{-5}$. e_σ is the unit vector in σ -direction. The dependences on q_1, q_3 and l in equation (4.59) are omitted to save space.

With this, we have all necessary expressions to calculate the pion-loop contribution to a_μ in sQED. Comparing the obtained result to (4.39), we now know that the four-point function was properly included as well. We will show the calculated values in section 4.7.

Now, we are able to change form factors without risking to endanger our numerics. We cannot include the $\pi\pi\gamma\gamma$ -vertex in our approach yet, so we have to restrict our calculations to the diagrams $C3$ and $C4$. For this, we only consider \mathcal{D}^1 and \mathcal{D}^2 . Since this subgroup is gauge dependent, we have to keep in mind that all results we produce can only be considered interim results that will become meaningful, when we include the missing diagrams $C1$ and $C2$.

Before we calculated the a_μ contribution with our approach, we wanted to observe the behavior of the result for different form factors. We performed calculations with

$$\mathcal{F}_{VMD1}^{\pi\pi\gamma}(p_1, p_2) = \frac{M_V^2}{(p_2 - p_1)^2 + M_V^2} \quad (4.60)$$

and

$$\mathcal{F}_{VMD2}^{\pi\pi\gamma}(p_1, p_2) = \frac{M_V^2}{(p_2 - p_1)^2 + M_V^2} \cdot \frac{M_V^2}{\frac{(p_1 + p_2)^2}{4} + M_V^2}. \quad (4.61)$$

The first form factor corresponds to a VMD model where only the photon momentum dependence is considered. For the additional dependence on the relative pion

momentum, we use $\mathcal{F}_{VMD2}^{\pi\pi\gamma}$. Qualitatively, this form factor is very close to our form factor $\mathcal{F}_{DSE/BSE}^{\pi\pi\gamma}$, corresponding to the dark green blob in Fig.4.12.

Finally, we calculated a_μ^{C3+C4} with $\mathcal{F}_{DSE/BSE}^{\pi\pi\gamma}$. The form factor was evaluated on a grid and fitted. We used a linear fit and a spline interpolation in the calculations.

The results we obtained are presented and discussed in the next section.

4.7 Results and Discussion

Before we present our results, we want to give a short overview of the values we calculate. First we consider the subgroup C of the scalar QED pion-loop diagrams with bare vertices to test our numerics. For this we include the bare $\pi\pi\gamma\gamma$ -vertex. Then we continue with a subgroup consisting of the diagrams $C3$ and $C4$, since these are the diagrams we are able to evaluate in our approach at the moment. We try to apply a simple VMD model, depending on the photon momenta q_i and k . Then we extend that model with a dependence on the relative pion momenta $(p_1 + p_2)/2$. Finally we deploy the DSE/BSE form factors. We performed all calculations in Landau and in Feynman gauge.

The first result we want to present is the full group C contribution to a_μ in sQED. This value has to be compared to (4.39). Our result for C with the $\pi\pi\gamma$ form factor \mathcal{F}_{sQED} is

$$a_\mu^C = 452.6(1.7) \quad (4.62)$$

in Landau gauge, and

$$a_\mu^C = 453.6(2.8) \quad (4.63)$$

in Feynman gauge. As before, the errors given for all of our results merely represents the numerical uncertainty of the integration, and do not represent the accuracy of the used method to calculate a_μ .

The comparison of (4.62) and (4.63) with (4.39) shows a reasonable good agreement. The difference to (4.39) is less than four percent. Since Ref. [32] did not specify their input parameters, we are not able to compare them. However, it is possible that, for very high values for the radii of q_1, q_3 and l at the same time, the precision of our code is exceeded. It is possible that this is the reason for the discrepancy. We tested two different code implementations and this behavior was only found in one of them. The results for the DSE/BSE form factor were the same for both codes, so we assume that the problem does not arise in these calculations, and the discrepancy is not important for our further analysis.

Now we restrict our calculations to the $C3$ and $C4$ contributions. Again, we start with the bare vertex, respective with the form factor \mathcal{F}_{sQED} . The obtained values are listed in table I. We clearly see that gauge invariance is broken for all tested form factors. However, the behavior when we compare the results obtained by using different form factors is the same. The results for Landau gauge are always bigger than the results in Feynman gauge by a factor of approximately five.

Since both sQED results for $C3 + C4$ are smaller than the full group C result, but rise with a lower gauge fixing parameter ξ , we assume that a gauge exists, where

Form factor \mathcal{F}	$a_\mu [\times 10^{11}]$		
	$\xi = 1$	$\xi = 0$	$\xi = -3.01$
\mathcal{F}_{sQED}	18.6(1.8)	101.5(1.2)	447.7(4.9)
\mathcal{F}_{VMD1}	-670.1(1.2)	-525.0(1.0)	1258.8(2.2)
\mathcal{F}_{VMD2}	8.1(0.2)	27.3(0.2)	147.5(0.5)
$\mathcal{F}_{DSE/BSE}^{lin}$	6.6(0.2)	34.1(0.2)	224.0(0.7)
$\mathcal{F}_{DSE/BSE}^{spl}$	7.3(0.4)	34.5(0.4)	222.5(1.1)

Table I: Results for the $C3$ and $C4$ contributions to a_μ in Landau ($\xi = 0$), Feynman ($\xi = 1$) and the special gauge $\xi = -3.01$, where $C3$ and $C4$ reproduce the whole result for C , for different form factors. .

the full C result is reproduced by $C3$ and $C4$. We tested different parameters ξ , see Fig.4.17, and found $\xi = -3.01$. This gauge produces the result

$$a_{\mu,sQED}^{C3+C4} = 447.7(4.9) \times 10^{-11}, \quad (4.64)$$

which overlaps with (4.62) and (4.63), if we include the errors. Now, we can neglect the contributions of $C1$ and $C2$. The obtained results in this gauge should be representative for the whole group C , so we tested all form factors with $\xi = -3.01$ as well.

The simple VMD ansatz \mathcal{F}_{VMD1} shows catastrophic behavior in all gauges. We clearly see that the results have the wrong sign in Landau and Feynman gauge, and that the obtained values are too large. The ansatz breaks the WTI (4.5), so any value extracted by using the derivative of the four point function is random.

We try to improve the situation by extending the form factor with a second factor, depending on the relative momentum $(p_1 + p_2)/2$. It is a reasonable assumption that this produces a more realistic behavior than the simple VMD model, since the full form factor includes this dependence. The form factor \mathcal{F}_{VMD2} behaves better than the previous result by far. The sign got fixed and the order of the contributions seems more reasonable. As expected in a VMD model, the numerical value is suppressed compared to the case of bare vertices.

The values obtained by applying the DSE/BSE form factor are basically the same for both the linear fit and the spline interpolation of the calculated data points. We see that the findings for the extended VMD model are already in a range comparable to our result. We interpret the behavior as an indication that it is important to include the relative momentum dependence.

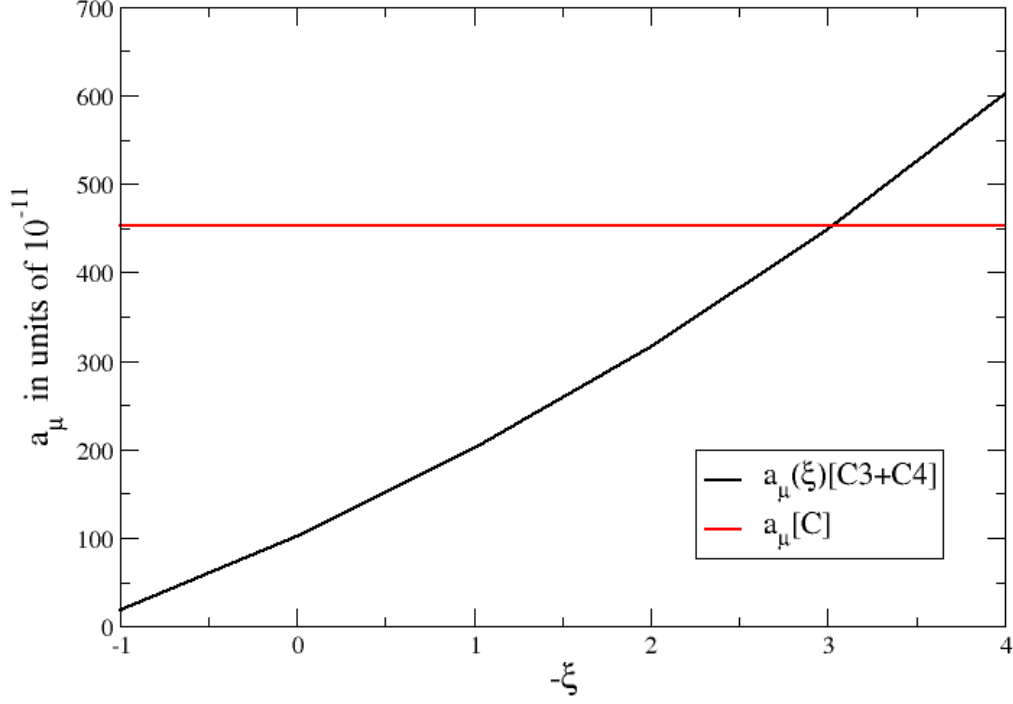


Figure 4.17: Behavior of a_μ^{C3+C4} , depending on the gauge parameter ξ . We plot results in different gauges versus the negative gauge parameter. The errors of the calculated a_μ are omitted. At approximately $\xi \approx -3.01$, the full value of a_μ^C , represented by the red line, is reproduced by the subgroup $C3 + C4$.

For now, we treat the result $a_\mu^{C3+C4}[\xi = -3.01]$ as the full contribution a_μ^C in our approach.

$$a_\mu^C = a_\mu^{C3+C4}[\xi = -3.01] = 222.5(1.1) \quad (4.65)$$

We take the spline interpolated result since it provides a more accurate representation of the form factor than the linear fit. Compared to the bare sQED result, the value is suppressed, as expected. However, the overall contribution of all pion-loop diagrams in sQED [32] is smaller by at least one order of magnitude, even for bare vertices, and most importantly negative,

$$a_{\mu, sQED}^{\pi-loop} = -0.0383(20) \left(\frac{\alpha}{\pi}\right)^3 \approx -48.0 \times 10^{-11}. \quad (4.66)$$

To compare results with this quantity and arrive at a final result $a_{\mu,DSE/BSE}^{\pi-loop}$, we would first have to include group A and B .

Another manifestation of the gauge dependence that should be mentioned, is the fact that our results depend on the momentum routing. We already mentioned two different possible routings, depicted in Fig.4.15 and Fig.4.16. When we are able to include the diagrams $C1$ and $C2$, and calculate C directly, we will use these routings to test the gauge invariance of the group. This dependence renders it almost impossible to compare the obtained results to any reference values. This is one reason, why we had to take so many steps to check our numerics. To be sure about the results in our approach, we used two independent code implementations.

In near future, we are going to be able to include the missing groups A , B and the diagrams $C1$, $C2$ and compare results to other approaches, with the help of an approach to Compton scattering of baryons, which we will apply to pions [33, 34]. We will present a more detailed explanation of the expansion of the photon four-point function, where we will further elaborate on the pion-loop diagrams we have to include in our calculations. Because of the limited time for this thesis, it was not possible to include these necessary tasks yet.

5 Conclusion

In this thesis, we wanted to investigate the pion-loop contribution to the anomalous magnetic moment of the muon, a_μ . Firstly, we elaborated on the historical background of the particle property 'anomalous magnetic moment'. Afterwards, we wanted to give a brief reminder of the property magnetic moment. Next, we gave an example of an experimental extraction method, and an experimental value for a_μ .

Then, we summarized the contributions to the anomalous magnetic moment in the Standard Model, and give reference values for all components considered so far. We compared the experimental and currently accepted theoretical results.

With the current situation outlined, we proceeded to explain the framework we used. We gave a schematic road map of how to calculate the quark propagator in Rainbow-Ladder truncation and briefly explained the truncation we apply. We introduced the Bethe-Salpeter Equation for the G -matrix and outlined the steps necessary to extract the BSEs for the T -matrix, the Bethe-Salpeter amplitude and the quark-photon vertex. Concluding chapter 3, we outlined the calculation of the hadronic vacuum polarization as an example of calculations related to a_μ in the DSE/BSE framework.

The next step was to address the real topic of this thesis, the hadronic light-by-light scattering contribution to the anomalous magnetic moment of the muon. We started with an explanation of the projector used to extract the anomalous magnetic moment from the muon-muon-photon vertex. To define the projection method, we introduced Ward-Takahashi Identities. We compared the expansion of the photon four-point function in effective field theories to our approach and motivated the analysis of the pion-loop contributions, even though they are not generically generated in our scheme to express the four-point function. We considered its finiteness and used the WTIs, to lower the naive degree of divergence of the photon four-point function. For completeness, we discussed the quark-loop contribution. We proceeded to explain the strategy we used to apply the pole-approximation for the T -matrix and identified our diagrams with contributions present in effective field theories, dressed with photon-meson form factors. We used the opportunity to explain and test part of our numerics with the known result of the pion exchange contribution. After this preparatory work, we finally elaborated on the charged pion-loop. We introduced the DSE/BSE form factor $\mathcal{F}_{DSE/BSE}$ and laid out the used numerical extensions compared to the pion exchange. To study the impact of VMD form factors without

and with dependence on the relative momentum of the pion, we calculated a_μ with \mathcal{F}_{VMD1} and \mathcal{F}_{VMD2} . We found that the breaking of the WTI by the form factor \mathcal{F}_1 lead to highly unreasonable results. However, the extended VMD ansatz showed acceptable behavior in both Landau and Feynman gauge. The value extracted from calculations with the form factor $\mathcal{F}_{DSE/BSE}$ were close to the extended VMD result and reinforces our believe that the impact of the relative momentum is important. We used the broken gauge invariance to find a gauge, where the full value of the contribution a_μ^C is produced by the diagram subgroup $C3 + C4$. In this gauge, we repeated the calculations for all form factors, and regard the results for the DSE/BSE form factor as our final result in this first approach for C . We compared it with the full group C of scalar QED and discussed its meaning in the full pion-loop contribution to the anomalous magnetic moment of the muon.

As a conclusion, we state that we are aware of the fact that we calculate only a subgroup of the pion-loop diagrams we should consider, and that this subgroup is not gauge invariant. We use this to extract a result for the full group C , even though we cannot calculate $C1$ and $C2$ yet. We also know, that, at the moment, the obtained results depend on the momentum routing. However, this problems will be resolved when we include the missing diagrams. The current results show the expected behavior when we include different form factors. Even though the interim results are not meaningful on their own, we can use them later on to extract the full pion-loop contribution to a_μ . We are confident that we can find a consistent approach to the $\pi\pi\gamma\gamma$ -vertex and resolve the problems stated here.

6 Bibliography

- [1] C. S. Fischer, T. Goecke, and R. Williams, “A fresh look at hadronic light-by-light scattering in the muon $g-2$ with the Dyson-Schwinger approach,” *Eur.Phys.J.* **A47** (2011) 28, [arXiv:1009.5297 \[hep-ph\]](#).
- [2] T. Goecke, C. S. Fischer, and R. Williams, “Hadronic light-by-light scattering in the muon $g-2$: a Dyson-Schwinger equation approach,” *Phys.Rev.* **D83** (2011) 094006, [arXiv:1012.3886 \[hep-ph\]](#).
- [3] T. Goecke, C. S. Fischer, and R. Williams, “Leading-order calculation of hadronic contributions to the muon $g - 2$ using the Dyson-Schwinger approach,” *Phys.Lett.* **B704** (2011) 211–217, [arXiv:1107.2588 \[hep-ph\]](#).
- [4] T. Goecke, C. S. Fischer, and R. Williams, “The role of momentum dependent dressing functions and vector meson dominance in hadronic light-by-light contributions to the muon $g - 2$,” *Phys.Rev.* **D87** no. 3, (2013) 034013, [arXiv:1210.1759 \[hep-ph\]](#).
- [5] F. Jegerlehner and A. Nyffeler, “The Muon $g-2$,” *Phys.Rept.* **477** (2009) 1–110, [arXiv:0902.3360 \[hep-ph\]](#).
- [6] T. Göckel, *Hadronic Contributions to the anomalous Magnetic Moment of the Muon*. PhD thesis, Universität Gießen, 2012.
- [7] S. Goudschmidt and G. Uhlenbeck, “Spinning electrons and the structure of spectra,” *Nature* **117** (1926) 264–265.
- [8] P. A. Dirac, “The Quantum theory of electron,” *Proc.Roy.Soc.Lond.* **A117** (1928) 610–624.
- [9] P. Kusch and H. M. Foley, “Precision measurement of the ratio of the atomic ‘ g values’ in the $^2p_{3/2}$ and $^2p_{1/2}$ states of gallium,” *Phys. Rev.* **72** (Dec, 1947) 1256–1257. <http://link.aps.org/doi/10.1103/PhysRev.72.1256.2>.
- [10] J. Schwinger, “On quantum-electrodynamics and the magnetic moment of the electron,” *Phys. Rev.* **73** (Feb, 1948) 416–417. <http://link.aps.org/doi/10.1103/PhysRev.73.416>.

- [11] T. Lee and C.-N. Yang, “Question of Parity Conservation in Weak Interactions,” *Phys.Rev.* **104** (1956) 254–258.
- [12] **Muon G-2 Collaboration** Collaboration, G. Bennett *et al.*, “Final Report of the Muon E821 Anomalous Magnetic Moment Measurement at BNL,” *Phys.Rev.* **D73** (2006) 072003, [arXiv:hep-ex/0602035](#) [[hep-ex](#)].
- [13] B. Roberts, “Status of the Fermilab Muon (g-2) Experiment,” *Chin.Phys.* **C34** (2010) 741–744, [arXiv:1001.2898](#) [[hep-ex](#)].
- [14] M. E. Peskin and D. V. Schroeder, *An Introduction To Quantum Field Theory (Frontiers in Physics)*. Westview Press, 1995.
- [15] T. Aoyama, M. Hayakawa, T. Kinoshita, and M. Nio, “Complete Tenth-Order QED Contribution to the Muon g-2,” [arXiv:1205.5370](#) [[hep-ph](#)].
- [16] A. Czarnecki, W. J. Marciano, and A. Vainshtein, “Refinements in electroweak contributions to the muon anomalous magnetic moment,” *Phys.Rev.* **D67** (2003) 073006, [arXiv:hep-ph/0212229](#) [[hep-ph](#)].
- [17] K. Hagiwara, R. Liao, A. D. Martin, D. Nomura, and T. Teubner, “ $(g - 2)_{\mu}$ and $\alpha(M_Z^2)$ re-evaluated using new precise data,” *J.Phys.G* **G38** (2011) 085003, [arXiv:1105.3149](#) [[hep-ph](#)].
- [18] J. Prades, E. de Rafael, and A. Vainshtein, “Hadronic Light-by-Light Scattering Contribution to the Muon Anomalous Magnetic Moment,” [arXiv:0901.0306](#) [[hep-ph](#)].
- [19] R. Alkofer and L. von Smekal, “The infrared behavior of QCD Green’s functions: Confinement, dynamical symmetry breaking, and hadrons as relativistic bound states,” *Phys. Rept.* **353** (2001) 281, [arXiv:hep-ph/0007355](#).
- [20] C. S. Fischer, “Infrared properties of QCD from Dyson-Schwinger equations,” *J. Phys.* **G32** (2006) R253–R291, [arXiv:hep-ph/0605173](#).
- [21] E. E. Salpeter and H. A. Bethe, “A Relativistic equation for bound state problems,” *Phys. Rev.* **84** (1951) 1232–1242.
- [22] N. Nakanishi, “Normalization condition and normal and abnormal solutions of the bethe-salpeter equation,” *Phys. Rev.* **138** no. 5B, (Jun, 1965) B1182–B1192.
- [23] P. Maris and P. C. Tandy, “The Quark photon vertex and the pion charge radius,” *Phys.Rev.* **C61** (2000) 045202, [arXiv:nucl-th/9910033](#) [[nucl-th](#)].

-
- [24] J. S. Ball and T.-W. Chiu, “Analytic Properties of the Vertex Function in Gauge Theories. 1.,” *Phys.Rev.* **D22** (1980) 2542.
- [25] S. J. Brodsky and J. D. Sullivan, “ w -boson contribution to the anomalous magnetic moment of the muon,” *Phys. Rev.* **156** (Apr, 1967) 1644–1647. <http://link.aps.org/doi/10.1103/PhysRev.156.1644>.
- [26] J. Aldins, T. Kinoshita, S. J. Brodsky, and A. Dufner, “Photon - photon scattering contribution to the sixth order magnetic moments of the muon and electron,” *Phys.Rev.* **D1** (1970) 2378.
- [27] E. de Rafael, “Hadronic contributions to the muon $g-2$ and low-energy QCD,” *Phys.Lett.* **B322** (1994) 239–246, [arXiv:hep-ph/9311316](https://arxiv.org/abs/hep-ph/9311316) [hep-ph].
- [28] J. Bijnens, E. Pallante, and J. Prades, “Analysis of the hadronic light by light contributions to the muon $g-2$,” *Nucl.Phys.* **B474** (1996) 379–420, [arXiv:hep-ph/9511388](https://arxiv.org/abs/hep-ph/9511388) [hep-ph].
- [29] M. Hayakawa and T. Kinoshita, “Pseudoscalar pole terms in the hadronic light by light scattering contribution to muon $g - 2$,” *Phys.Rev.* **D57** (1998) 465–477, [arXiv:hep-ph/9708227](https://arxiv.org/abs/hep-ph/9708227) [hep-ph].
- [30] M. Knecht and A. Nyffeler, “Hadronic light by light corrections to the muon $g-2$: The Pion pole contribution,” *Phys.Rev.* **D65** (2002) 073034, [arXiv:hep-ph/0111058](https://arxiv.org/abs/hep-ph/0111058) [hep-ph].
- [31] T. Hahn, “CUBA: A Library for multidimensional numerical integration,” *Comput.Phys.Commun.* **168** (2005) 78–95, [arXiv:hep-ph/0404043](https://arxiv.org/abs/hep-ph/0404043) [hep-ph].
- [32] T. Kinoshita, B. Niić, and Y. Okamoto, “Hadronic contributions to the anomalous magnetic moment of the muon,” *Phys. Rev. D* **31** (Apr, 1985) 2108–2119. <http://link.aps.org/doi/10.1103/PhysRevD.31.2108>.
- [33] G. Eichmann and C. S. Fischer, “Unified description of hadron-photon and hadron-meson scattering in the Dyson-Schwinger approach,” *Phys.Rev.* **D85** (2012) 034015, [arXiv:1111.0197](https://arxiv.org/abs/1111.0197) [hep-ph].
- [34] G. Eichmann and C. S. Fischer, “Nucleon Compton scattering in the Dyson-Schwinger approach,” *Phys.Rev.* **D87** no. 3, (2013) 036006, [arXiv:1212.1761](https://arxiv.org/abs/1212.1761) [hep-ph].

Erklärung

Hiermit erkläre ich, dass ich die vorliegende Master-Thesis selbstständig verfasst und keine anderen als die angegebenen Quellen und Hilfsmittel benutzt habe.

Giessen, den October 30, 2013

Jan Haas